Acta Pharmaceutica Sinica B 2026;16(1):503−521

Chinese Pharmaceutical Association
Institute of Materia Medica, Chinese Academy of Medical Sciences

Acta Pharmaceutica Sinica B

www.elsevier.com/locate/apsb
www.sciencedirect.com

ORIGINAL ARTICLE

# An innovative and stable mRNA-LNP microneedle vaccine elicits humoral and multifunctional cellular immune responses

**Xiaoxuan Hong[a,c,d,e], Xianfu Li[b], Xiaolu Han[b], Jinghu Lou[b], Yue Li[b], Jintao Lin[b], Yi Cheng[b], Haonan Xing[b], Hui Zhang[b], Xiwei Wang[b], Shuang Zhang[a,c,d,e], Nan Liu[b], Zengming Wang[b,*], Chunying Cui[a,c,d,e,*], Aiping Zheng[b,*]**

[a]*Department of Pharmaceutics, School of Pharmaceutical Sciences, Capital Medical University, Beijing 100069, China*
[b]*Beijing Institute of Pharmacology and Toxicology, Beijing 100850, China*
[c]*Beijing Area Major Laboratory of Peptide and Small Molecular Drugs, Beijing 100069, China*
[d]*Beijing Laboratory of Biomedical Materials, Beijing 100069, China*
[e]*Laboratory for Clinical Medicine, Capital Medical University, Beijing 100069, China*

Received 3 March 2025; received in revised form 13 May 2025; accepted 6 July 2025

**KEY WORDS**

Microneedle;
mRNA;
Lipid nanoparticles;
Mannose;
Stability;
Antigen-presenting cells;
Systemic humoral;
Cellularc immunity

**Abstract** During the COVID-19 pandemic, the use of lipid nanoparticles (LNPs) augmented the development of mRNA vaccines. However, their ultralow-temperature storage and transportation requirements, as well as their heavy reliance on injection by professional medical staff, have limited large-scale vaccination in many developing countries. Herein, we developed a simple and widely deployable microneedle (MN) vaccine delivery system (mLNP-man-MN) for mannose-modified LNPs (mLNP-man) loaded with mRNA encoding the SARS-CoV-2 spike receptor-binding domain by utilizing three-dimensional printing and polydimethylsiloxane micro molding methods. This delivery system is composed of a dissolvable polymer mixture that was optimized for high bioactivity by screening formulations *in vitro*. We have demonstrated that this MN system can maintain the physicochemical properties and bioactivity of the mRNA-LNP complex even when stored at 4 °C for at least one month or at 25 °C for two weeks. Moreover, mLNP-man-MNs target the epidermis and dermis, which are rich in antigen-presenting cells, thereby eliciting effective innate immune responses and inducing robust systemic humoral responses,

*Corresponding authors.
E-mail addresses: apzheng@163.com (Aiping Zheng), ccy@ccmu.edu.cn (Chunying Cui), wangzm.1986@163.com (Zengming Wang).
Peer review under the responsibility of Chinese Pharmaceutical Association and Institute of Materia Medica, Chinese Academy of Medical Sciences.

https://doi.org/10.1016/j.apsb.2025.10.006

as well as multifunctional cellular immunity in the spleen. Importantly, the MN system induced a certain level of pulmonary T-cell responses compared to those induced by intramuscular injections, thereby providing some protection against lung invasion by the SARS-CoV-2 pseudovirus in mice.



## 1. Introduction

The coronavirus disease 2019 (COVID-19) pandemic has severely impacted global socioeconomic and public health. With the widespread implementation of vaccination strategies, the gradual resumption of daily human activities signaled the advent of the post-pandemic era[1]. However, the threats posed by emerging and reemerging infectious diseases cannot be overlooked[2]. Therefore, the development of effective strategies to cope with potential pandemics is of paramount importance[3−7]. In the context of the COVID-19 pandemic, lipid nanoparticle (LNP)-encapsulated mRNA vaccines have shown considerable promise for revolutionizing life sciences and medical research. Their attributes include low risk of insertional mutagenesis, high safety, proven efficacy, rapid and scalable production capabilities, and cost-effectiveness[8]. These vaccines are currently being utilized to tackle new coronavirus variants, influenza, and herpes simplex virus[9−11], demonstrating their broad applicability and impact.

However, one of the primary limitations of mRNA vaccines is their poor stability, which typically requires storage and transportation under ultra-low temperature conditions (−80 °C)[12,13]. This stringent cold chain requirement poses challenges for global vaccine distribution, particularly in resource-limited regions[14−16]. Moreover, most vaccines are administered *via* intramuscular (IM) injection, which faces a series of challenges, including the instability of liquid formulations at ambient temperatures, requirements for trained healthcare personnel to administer vaccines, patient aversion to the administration route (needle phobia, injection site pain, and risk of unintended local or systemic immune reactions)[17,18], and risk of contamination (needle/injection site). These challenges reinforce the phenomenon of vaccination hesitancy. Therefore, there is an urgent need to develop a stable, alternative vaccine model that can improve vaccination efficacy and coverage in different populations.

In recent years, dissolvable microneedle (MN) transdermal drug delivery systems have rapidly evolved as cutting-edge alternatives to traditional vaccine administration methods. MNs are arrays of micrometer-sized needle-like projections that mechanically penetrate the stratum corneum of the skin and deploy vaccine components in the epidermis/dermis in a painless, minimally invasive fashion[19]. The skin is rich in dendritic cells (DCs) and macrophages. The abundance of these antigen-presenting cells (APCs), combined with the extensive interaction between the skin and lymphatic circulation, can induce a robust immune response[20]. Furthermore, vaccines utilizing MN technology enable individuals to self-administer them after minimal training. This approach mitigates the risk of cross-infection and reduces the burden on medical supplies[21]. Furthermore, the cutaneous immunity elicits an effective mucosal response that confers a significant advantage against respiratory pathogens[22−24]. For instance, the administration of vaccinia virus or a modified Ankara vaccinia virus *via* skin scratching has been demonstrated to be an effective method for preventing infection by respiratory pathogens in animal models[25,26]. In particular, the most successful vaccine in human history, the smallpox vaccine, was administered *via* the skin-scratching method, resulting in the worldwide eradication of the smallpox virus[27]. Therefore, MN-based delivery systems are emerging as promising strategies for vaccine administration.

In this study, we developed a simple and widely deployable mRNA-LNP MN vaccination strategy. The MN system is composed of LNPs loaded with mRNA encoding the SARS-CoV-2 spike receptor-binding domain (RBD) and a mixture of polyvinylpyrrolidone (PVP), Soluplus®, and sucrose (Fig. 1). These components synergistically form a stable protective layer on the nanoparticle surface, ensuring the structural and functional stability of the mRNA-LNP complexes during MN preparation and storage. The MN delivery system targets LNPs to the skin microenvironment with an immune response in mouse skin, directly targeting a large number of APCs to enhance LNP exposure. In addition, mannose-modified LNPs (mLNP-man) bind to mannose receptors on the surface of DCs and enhance LNP uptake by DCs, thereby stimulating robust innate and adaptive immune responses. Importantly, the MN delivery system also induces a certain pulmonary T-cell response compared to that induced when vaccines are delivered *via* the IM route, which is crucial for first-line defense against pulmonary viral infections such as COVID-19[28-31] (Fig. 1). Overall, the MN delivery of mLNP-man vaccines is a safe and promising strategy for SARS-CoV-2 immunization.

## 2. Materials and methods

### 2.1. Materials and animals

Fetal bovine serum (FBS), the SARS-CoV-2 (2019-nCoV) spike RBD recombinant protein and SARS-CoV-2 (D614G)-GFP-Luc pseudovirus were purchased from Vazyme Biotech Co., Ltd. (Beijing, China). 306Oi10 were purchased from MCE (HY-151507, Monmouth Junction, NJ, USA). 1,2-Dimyristoyl-rac-glycero-3-methoxypolyethylene glycol-2000 (DMG-PEG2000), cholesterol and sucrose were obtained from AVT Pharmaceutical Technology Co., Ltd. (Shanghai, China). 1,2-Dioleoyl-*sn*-glycero-3-phosphoethanolamine (DOPE) was purchased from SINOPEG (Xiamen, China). DMG-PEG2000-Mannose (DMG-PEG2000-man) was custom synthesized by Xi'an Ruixi Biological Technology Co., Ltd. (Xi'an, China). Quant-IT™ Ribogreen RNA Assay Kit and murine granulocyte-macrophage colony-stimulating factor (GM-CSF) were purchased from Invitrogen (Carlsbad, CA, USA). $CD3^+$ T cell isolation kit was purchased from Xiamen Immocell Biotechnology Co., Ltd. (Xiamen, China). Polyvinylpyrrolidone (PVP) was purchased from Ashland Chemical Trading Co., Ltd. (Shanghai, China). Soluplus® was purchased from BASF (Shanghai, China). Polyethylene glycol

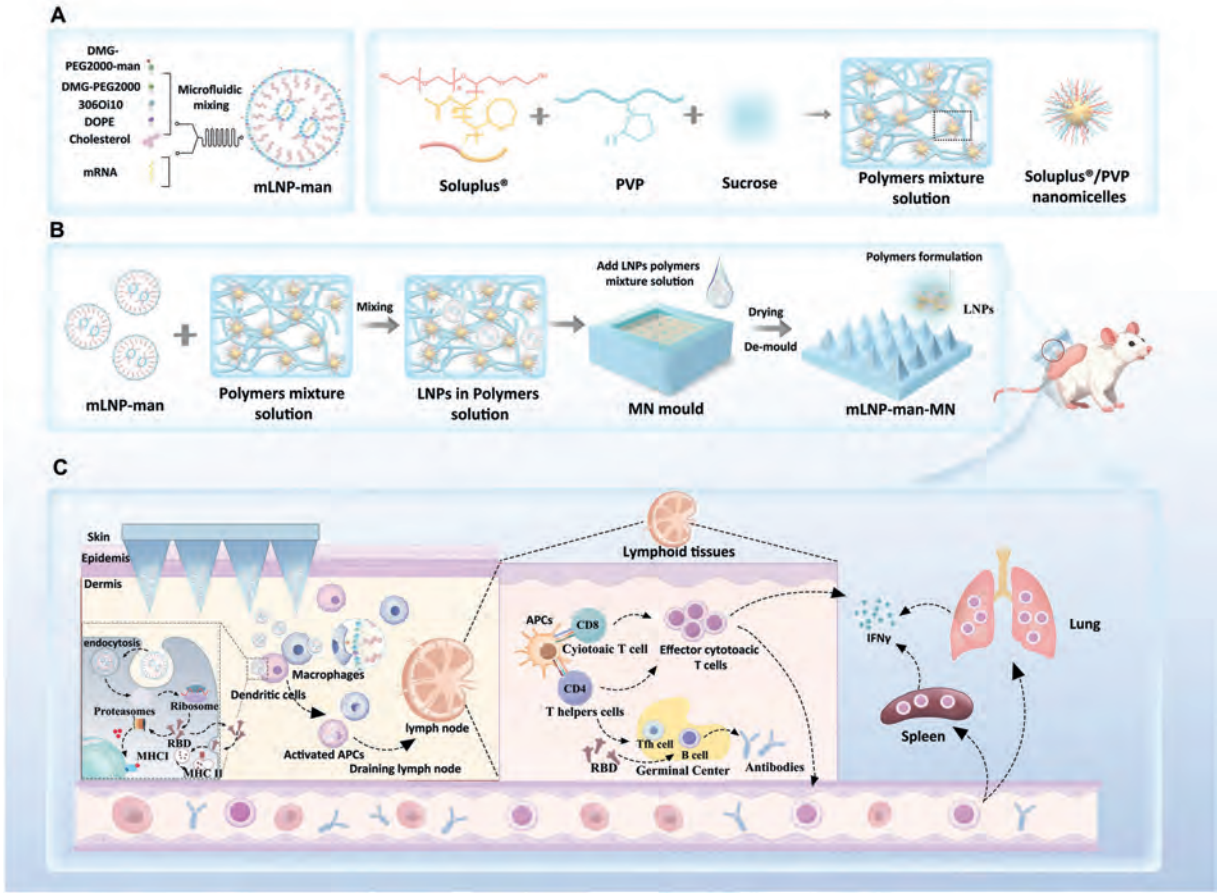


**Figure 1** Schematic representation of the preparation process and *in vivo* induction of immune responses for the innovative stabilized mRNA-LNP microneedle vaccines. (A) Schematic diagram of the composition of mLNP-man and polymers mixture solution. (B) Schematic representation of the preparation of mLNP-man vaccines loaded microneedles (mLNP-man-MN). (C) Schematic diagram of mLNP-man-MN immunization inducible humoral and multifunctional cellular immune responses.

(400) diacrylate (PEG(400)DA) and polyethylene glycol (600) diacrylate (PEG(600)DA) were purchased from Shanghai Aladdin Biochemical Technology Co., Ltd. (Shanghai, China). Collagenase D was purchased from Roche (Basel, Switzerland). A CCK-8 kit was obtained from Beyotime (Shanghai, China). All the antimouse antibodies were purchased from BioLegend (San Diego, CA, USA). HRP-labeled antimouse IgG, IgG1, and IgG2a were purchased from Abcam (Cambridge, MA, USA). Dulbecco's modified Eagle's medium (DMEM) was purchased from HUANKE (Beijing, China).

BALB/c mice were purchased from SPF Biotechnology Co., Ltd. (Beijing, China). H11-K18-hACE2 mice (Strain No. T037657) were purchased from GemPharmatech (Nanjing, China). All experimental procedures were executed according to the protocols approved by the Institutional Animal Care and Use Committee of the Academy of Military Medical Sciences, under the approval number IACUC-DWZX-2023-659.

### 2.2. *LNPs preparation and characterization*

The lipid components were dissolved in ethanol to obtain a lipid mixture working solution. The molar ratio of lipids for LNPs was 35:16:46.5:2.5, comprising 306Oi10, DOPE, cholesterol, and DMG-PEG2000. The mRNA was diluted with RNase-free 25 mmol/L sodium citrate buffer (pH 4.0), resulting in a final weight ratio of lipid:mRNA of 10:1 (3:1 mol/L). Subsequently, the lipid and mRNA solutions were rapidly mixed in a microfluidic device (Shanghai Pengzan Biotechnology Co., Ltd., Shanghai, China) at a 1:3 flow rate ratio and 12 mL/min total flow rate. The obtained LNPs were buffer exchanged (20 mmol/L Tris buffer) three times in 100 kDa ultrafiltration tubes (Millipore, Burlington, MA, USA).

The particle size distribution and zeta potential of the LNPs were determined by dynamic light scattering (DLS) using a Malvern Zetasizer Nano (Malvern Panalytical, ZS90, Malvern, UK). The morphology of LNPs was observed under a transmission electron microscope (TEM) (HITACHI, Tokyo, JPN). The mRNA encapsulation efficiency was quantified using the Quant-iT™ RiboGreen RNA Assay Kit (Invitrogen).

### 2.3. *In vitro maturation of bone marrow dendritic cells (BMDCs) and T cells*

Bone marrow from C57BL/6 male mice (6−8 weeks old) was taken, lysed for erythrocytes, washed, and resuspended in RPMI 1640 medium (containing 10% FBS) with GM-CSF. The cells

were incubated at 37 °C in a 5% $CO_2$ incubator with fluid changes every other day. After 7–8 days of culture, the suspended and loosely adherent cells were BMDCs, and most of the adherent cells were bone marrow-derived macrophages (BMDMs).

The extracted BMDCs were inoculated into 12-well plates and treated with PBS or LNPs for 24 h. Then the cells were stained with anti-mouse BV605-CD11c, APC-CD40, BV421-CD80, APC Cy7-CD86, PE-MHC I and PerCP-MHC II antibodies for 30 min, rinsed with PBS, resuspended and detected by a flow cytometer (Invitrogen, Attune NxT, Carlsbad, CA, USA).

Spleens were removed from C57BL/6 male mice (6–8 weeks old) and strained through a 70-μm cell strainer to obtain a single-cell suspension. Erythrocytes were lysed with an Ammonium-Chloride–Potassium (ACK) lysis buffer. $CD3^+$ T cells were isolated using a $CD3^+$ T cell isolation kit according to the manufacturer's protocol. BMDCs treated with LNPs for 24 h were collected and co-cultured with T cells at a ratio of BMDCs to T cells of 1:5 for 72 h. Then the cells were stained with anti-mouse Pacific Blue-CD3, APC-CD4, PE Cy7-CD8 and PE-CD69 antibodies for 30 min and analyzed by flow cytometry (Invitrogen).

### *2.4. In vitro transfection efficiency of LNPs in BMDCs and BMDMs*

Extracted BMDCs and BMDMs were inoculated in multiwell plates and incubated to appropriate confluence. Replace with low serum Opti-MEM® solution and add LNPs, incubate for 6 h and then replace with complete medium. After 24 h of incubation at 37 °C and 5% $CO_2$, cells were rinsed with PBS, centrifuged, and enhanced green fluorescent protein (eGFP) positive cells were analyzed by flow cytometry (Invitrogen).

### *2.5. Preparation and characterization of mRNA-LNPs MN vaccines*

High-precision MN master templates with lengths and widths of 1000 and 450 μm, respectively, arranged in a 12 × 12 array, were fabricated using a commercial digital light processing (DLP) microArch® 3D printer (BMF Material, S140, Chongqing, China). Subsequently, an elastomeric polydimethylsiloxane (PDMS, base material to hardener ratio 10:1) was employed to create MN moulds, resulting in the formation of flexible moulds with pyramidal wells. The MN patches were prepared using a vacuum-assisted casting method[32]. Specifically, the LNPs were suspended in a Tris solution containing 10%–20% PVP, Soluplus® and sucrose. It was then added to a PDMS mold and evacuated (−1 bar, 2 min) to fill voids. Air bubbles were removed and the sample was concentrated in a desiccator for 2 h. This vacuum filling and concentration were repeated to get the proper needle length. Subsequently, a PEGDA solution (1:1 mix of PEG (400) DA and PEG (600) DA with 1% TMO) was added to the mold and the same process was repeated. After 1 min UV cross-linking at 405 nm with a portable light, the films were peeled for mRNA-LNP MN vaccines.

### *2.6. Characterisation of MNs*

#### *2.6.1. Physical morphology*

The physical morphology of MNs was observed using handheld microscope (Wuxi Dimension Optical Co, Ltd., Wuxi, China), fluorescence microscope (Olympus, Tokyo, Japan), scanning electron microscope (SEM) (Zeiss, Jena, Germany), optical coherence tomography angiography (OCT) (Optoprobe, Micro-VCC, London, England), and micro computed tomography (micro-CT) (Kunshan Yxford Precision Instrument Co., Ltd., 600 M, Kunshan, China).

#### *2.6.2. Mechanical strength*

The mechanical strength of MNs was evaluated using a texture analyzer (Shenzhen Meister Optoelectronics Technology Co., Ltd., MTS C42.502y, Shenzhen, China). In summary, the MNs were affixed to the metal platform of the texture analyzer with double-sided adhesive tape, with the MN tips oriented upwards. The probe was moved vertically towards the MN patch at a constant speed of 0.05 mm/min. The initial distance between the MN tip and the sensor was set at 0.5 cm, with a trigger force of 0.05 N. The measurement was terminated when the contact force reached 70 N, with the displacement and the corresponding force on the MNs recorded, and a force-displacement curve plotted.

#### *2.6.3. Needle tip distribution and insertion capability*

The LNPs were labeled with DiD as detailed in Section 2.5. The distribution of LNPs in MNs was observed using a fluorescence microscope (Olympus). In order to observe the penetration of the MNs into the skin *in vitro*, OCT was used to scan the state of MNs before and after insertion into the pig skin. Subsequently, the skin samples were fixed in 4% tissue fixative and sent to Beijing Mango Jingyan Biotechnology Co., Ltd. for histological examination.

#### *2.6.4. In vitro dissolution experiments of MNs*

The prepared MNs were inserted into a 4% agarose gel, and the microneedles were removed at different time points (0 or 30 s, 1, 2 and 3 min). The dissolution of the tip layer of the MNs was observed under a fluorescence microscope (Olympus).

### *2.7. The stability of mRNA-LNPs in the MNs*

The polymer solution was weighed and combined with the LNP suspension in order to achieve an appropriate ratio of polymers to mRNA mass. After drying to form MNs, they were redissolved in Tris solution and assayed for particle size and encapsulation efficiency. Subsequently, the mRNA was separated from the LNPs in the sample using a Triton solution. The integrity of the mRNA was confirmed using agarose gel electrophoresis and an automated capillary electrophoresis instrument (Hangzhou Houze Biotechnology Co., Ltd., Hangzhou, China). The transfection efficiency of LNPs in MNs was also evaluated in HEK293T cells. The procedure is described in Section 2.4. Simultaneously, the morphology of LNPs after redissolution in MNs and their state following solidification into MNs were observed using TEM (HITACHI) and SEM (Zeiss), respectively.

### *2.8. Evaluation of dynamic changes in APCs at immune sites*

To evaluate the dynamic changes in APCs at the injection site, BALB/c mice (6–8 weeks old) were intramuscularly (IM) or MN vaccinated with mLNP or mLNP-man vaccines and were euthanized 1, 7, and 14 days post-administration. Muscle tissues from the injection sites and skin tissues from the MN administration sites were collected separately and incubated in PBS containing 0.2% (*w*/*v*) collagenase D and 10 U/mL DNase I at 37 °C for 2 h to facilitate tissue digestion and subsequent extraction of single-cell suspensions. Cell blocking was then performed using an

anti-mouse CD16/CD32 antibody for 20 min. Staining was carried out using anti-mouse BV605-CD11c, APC-CD11b, PE-F4/80 and BV421-CD80 antibodies. Finally, the samples were analyzed by flow cytometry (Invitrogen).

### 2.9. *In vivo APCs lymphoid migration and maturation*

BALB/c mice (6−8 weeks old) were vaccinated with mLNP or mLNP-man vaccines by IM or MN, respectively, and the mice were euthanized 24 h after vaccination. Single-cell suspensions were prepared by removing mouse inguinal lymph nodes and stained with anti-mouse BV605-CD11c, APC-CD11b, and PE-F4/80 antibodies for 30 min at 4 °C. Data were then collected using a flow cytometer (Invitrogen) and analyzed with FlowJo software (TreeStar, v10.8.1, Ashland, OR, USA). At the same time, the inguinal lymph nodes were removed to make immunofluorescence sections, which were observed under a fluorescence microscope (Olympus) and images were captured.

Similarly, BALB/c mice (6−8 weeks old) were euthanized 7 days after inoculation. Mouse lymph node cells were collected and stained with anti-mouse PE/Cy7-CD11c, BV421-CD80, and APC/Cy7-CD86 antibodies to assess dendritic cell maturation, and with anti-mouse BV421-CD3 and PE-CD69 antibodies to assess lymph node T cell activation.

### 2.10. *Animal immunization*

The female BALB/c mice (6-week-old) were randomly divided into 3 groups ($n = 5$) and immunized with mLNP or mLNP-man by MNs (mLNP-MN or mLNP-man-MN) and mLNP-man by IM (mLNP-man-IM). Naive mice were used as controls. The administered group contained the same dose of 8 μg mRNA. The MNs were inserted vertically into the bare dorsal skin of the mice and held in place for 15 min, after which the MNs were torn off once they had completely dissolved. Each group received primary immunization on Days 0 and 14, with booster immunization on Day 28. Serum samples were taken on Days 21 and 42.

### 2.11. *ELISA*

Commercial SARS-CoV-2 RBD protein was diluted to 1 μg/mL in coating buffer (pH 9.6) and coated on 96-well plates at 4 °C overnight. Next, wash the plates 3 times with PBS-T (0.05% Tween-20), add 200 μL blocking buffer (2% BSA in PBST) per well, incubate 1 h, then wash again. Dilute serum samples in PBS-T with 0.2% BSA. Incubate at 37 °C for 2 h, wash 5 times with PBST, add 100 μL HRP-conjugated anti-mouse IgG, IgG1, IgG2a, incubate 1 h, wash 5 times, add 200 μL TMB substrate, incubate 25 min in the dark, stop with 2 mol/L sulfuric acid, and read OD at 450 nm using a microplate reader (Invitrogen, Varioskan LUX, Waltham, MA, USA).

### 2.12. *Analysis of Tfh cells and GC B cells*

Twenty-one days post-immunization, the mice were euthanized, and the inguinal lymph nodes were collected to prepare single-cell suspensions. Tfh cells were stained with anti-mouse APC-CD4, BV421-CXCR5 and FITC-PD-1 antibodies. GC B cells were stained with anti-mouse BV421-CD19, APC-FAS, and PE-GL7 antibodies. After staining, data were acquired using a flow cytometer (Invitrogen) and analyzed with FlowJo software (TreeStar).

### 2.13. *Detection of memory T cells*

Mice immunized for 42 days were euthanized and the spleen, lymph nodes and lungs were isolated to obtain single cell suspensions. $1 \times 10^6$ spleen and lung lymphocytes were inoculated into 24-well plates and incubated with a pool of 5 μg/mL RBD peptide for 48 h at 37 °C. Spleen lymphocytes and lymph node single-cell suspensions were harvested and stained with anti-mouse BV421-CD3, APC-CD4, APC/Fire™ 750-CD8, PE-CD44 and BV510-CD62L antibodies. Lung single-cell suspensions were stained with PE-CD3 and APC-CD44 antibodies. Data were acquired using a flow cytometer and analyzed with FlowJo software (TreeStar). In addition, the proliferation of splenocytes was measured using the CCK-8 assay.

### 2.14. *ELISpot assay*

To assess the level of cellular immune response produced by immunized mice, $5 \times 10^5$ of the spleen single cell suspensions and $2 \times 10^5$ of the lung single cell suspensions described above were inoculated into mouse IL-4 or IFN-γ pre-coated 96-well plates and incubated with a pool of 5 μg/mL of RBD peptide for 22 h. After incubation, the remaining steps were performed according to the respective protocols. Finally, the number of IL-4 spots and IFN-γ spots was counted using an ELISpot reader (Mabtech AB, Mabtech IRIS, Nacka Strand, Sweden).

### 2.15. *Intracellular cytokine staining (ICS)*

The above mouse spleen lymphocytes were inoculated into 96-well plates at $1 \times 10^6$ per well, then incubated with 5 μg/mL of RBD peptide pool at 37 °C for 1 h. Brefeldin A (1 μg/mL) was added and incubated for 5 h more. The cells were collected and stained for surface markers with anti-mouse BV421-CD3, APC-CD4, APC/Fire™ 750-CD8 in the dark for 30 min. For intracellular cytokine staining, the cells were stained with anti-mouse PE-IFN-γ, PE-TNF-α, PE-IL-4, and PE-IL-2 in the dark for 1 h. After washing, the cells were analyzed using a flow cytometer (Invitrogen).

### 2.16. *Pseudovirus neutralisation experiment*

Pseudovirus neutralization experiments were performed as previously reported in the literature[33]. Briefly, diluted samples were incubated with pseudoviruses (SARS-CoV-2 (D614G)-GFP-Luc) at 37 °C for 1 h. After incubation, the serum-pseudovirus mixtures were transferred to 96-well plates containing HEK293T-ACE2 cells and incubated at 37 °C in 5% $CO_2$ for 48 h. 100 μL of luciferase detection reagent was added to each well, and the plates were incubated at room temperature for 2 min. Luciferase activity was measured using a microplate reader (Invitrogen).

### 2.17. *Pseudovirus virus attack challenge*

The female H11-K18-hACE2 mice (7-week-old) were inoculated with mLNP-man by IM and MN, respectively, and the immunization procedure was consistent with BALB/c mice. Serum was collected on Day 42 and mice were infected by intratracheal instillation of 40 μL SARS-CoV-2 (D614G)-GFP-Luc. On Day 44, mice were euthanized and their lung tissue was collected. Mouse lung tissues were imaged *ex vivo* by the small animal *in vivo* imager (CLINX, IVScope 8200, Shanghai, China). Subsequently,

lung single-cell suspensions were prepared and the frequency of GFP-positive cells was analyzed using flow cytometry (Invitrogen). Lung tissues were also paraffin-embedded and sectioned to observe the fluorescence distribution of pseudoviruses.

### 2.18. Statistical analysis

Statistical analyses were performed using GraphPad Prism software (GraphPad Inc., v10.0.2, La Jolla, CA, USA). An unpaired two-tailed *t*-test was used for comparison between the two groups. One-way ANOVA was used to assess the significance of differences between groups. Significance levels were defined as follows: $*P < 0.05$, $**P < 0.01$, $***P < 0.001$, $****P < 0.0001$; ns, not significant.

## 3. Results

### 3.1. Preparation and characterization of mLNP-man

We designed a plasmid encoding the RBD protein and successfully prepared an mRNA using *in vitro* transcription (IVT) (Supporting Information Fig. S1). Using a microfluidic mixing strategy, DMG-PEG2000-man was formulated with other lipid components into mLNP-man (Fig. 2A). To determine the optimal assembly molar ratio of DMG-PEG2000-man, LNPs with different molar ratios of DMG-PEG2000-man (0, 0.5%, 1.0%, 1.5%, and 2.0%) were prepared. The DC 2.4 cell *in vitro* transfection results indicated that LNPs with a DMG-PEG2000-man molar ratio of 1.5% exhibited the best transfection efficiency (Supporting Information Fig. S2). After the assessment of factors, such as particle size, encapsulation efficiency, and *in vitro* transfection efficiency (Fig. S2), a DMG-PEG2000-man molar ratio of 1.5% was selected for the preparation of mLNP-man. TEM images showed that both the mLNP and mLNP-man exhibited a uniform spherical morphology (Fig. 2B). The DLS results (Fig. 2C) showed that both LNPs displayed relatively uniform sizes (100−150 nm) with good monodispersity (PDI <0.2). In addition, both LNPs had neutral or weakly positive zeta potentials and high mRNA encapsulation efficiency (>90%) (Fig. 2D).

Subsequently, we verified whether mLNP and mLNP-man facilitated mRNA delivery into primary APCs. BMDCs and BMDMs were used for *in vitro* expression studies. C57BL/6 mice were selected for induction and extraction of BMDCs and BMDMs (Fig. 2E). The results demonstrate that mLNP-man had a higher transfection efficiency in BMDCs and BMDMs (Fig. 2F). This enhanced efficiency is likely attributed to the mannose on the surface of LNPs, which are specifically recognized and internalized by the mannose receptor (MR) expressed on APCs, thereby facilitating the uptake and subsequent expression of LNPs by APCs[34]. To further explore the mLNP-man-induced antigen-presenting and dendritic cell maturation capacity, we incubated PBS, mLNP, and mLNP-man with BMDCs for 24 h. Flow cytometry was performed to detect the upregulation of immune activation molecules such as CD40, CD80, CD86, MHC I and MHC II in BMDCs. The results showed that the proportions of $CD40^+$ $CD11c^+$, $CD80^+$ $CD11c^+$, and $CD86^+$ $CD11c^+$ cells in the mLNP-man group were significantly higher than those in the mLNP group (Fig. 2G and Supporting Information Fig. S3). The upregulation of these surface markers indicated that DCs transitioned from an immature resting state to a mature active state, initiating an effective immune response that is crucial for activating subsequent T cell-mediated immunity. Furthermore, both mLNP and mLNP-man were able to promote the expression of MHC I and MHC II molecules on BMDCs (Fig. 2H and Fig. S3). There was no significant difference in promoting MHC I expression between the two groups. However, in terms of promoting MHC II expression, the percentage of $CD11c^+$ MHC $II^+$ cells in the mLNP-man group was significantly higher than that in the mLNP group, indicating that mannose-modified LNPs primarily enhance the antigen presentation function of BMDCs through the MHC II pathway.

To investigate how mannose-modified LNPs influence T cell priming, we co-cultured BMDCs treated with mLNP and mLNP-man with naive T cells for 72 h, followed by flow cytometry analysis to assess the expression of the T cell activation marker CD69. The results demonstrated that both mLNP and mLNP-man were capable of inducing early activation of $CD4^+$ and $CD8^+$ T cells. Furthermore, compared to mLNP, mLNP-man exhibited a stronger activating effect on both T cell subsets (Fig. 2I and Supporting Information Fig. S4). Moreover, the BMDCs maintained robust viability after incubation with different concentrations of mLNP and mLNP-man for 24 h (Supporting Information Fig. S5A). In addition, the mLNP and mLNP-man exhibited good hemocompatibility (Fig. S5B).

### 3.2. Preparation and characterization of the mLNP-man-MN

MNs loaded with mLNP-man were prepared in three steps: customization of the MN master mold, preparation of the PDMS female mold, and fabrication of dissolvable mLNP-man-MN. The MN master mold was customized using projection micro-stereolithography (PμSL) technology, which allows for rapid delivery of structural design and mold fabrication to meet different patient needs. In this study, we designed a pyramid-shaped MN, which has sharper edges and penetrates the stratum corneum more readily[35]. PDMS female molds were prepared using the membrane-turning method based on the MN master molds (Fig. 3A). mLNP-man was then mixed with a soluble polymer at the appropriate mass ratio, and the mixture was loaded into the MNs using vacuum casting (Fig. 3B).

As shown in Fig. 3C, the MN patch consisted of $12 \times 12$ microneedles precisely arranged in a regular pyramidal shape, with each microneedle equally spaced. SEM images of the MNs show the fine structure in different views (Fig. 3D), and the 3D printed layer-by-layer outlines can be seen when magnified. Quantification of the relative heights of the MNs using 3D pseudo-color maps displayed using micro-CT imaging revealed minimal differences, with a bottom length of 450 μm and a height of 1000 μm (Fig. 3E). This demonstrated the uniformity and reproducibility of the mLNP-man-MN formulation. To visualize the distribution of LNPs within the MNs, we used the red fluorescent dye DiD to label the LNPs and prepared mLNP-man-MNs. As illustrated in Fig. 3F, the red fluorescence, indicative of labeled mLNP-man, was predominantly concentrated at the tips of the MNs. Conversely, the base of the needles exhibited virtually no fluorescence signal, confirming that mLNP-man did not penetrate the substrate layer during the drying phase. The encapsulated mRNA loading in the MNs was then measured. Very little variation between batches was observed, with each MN loading of approximately $2.17 \pm 0.18$ μg mRNA (Supporting Information Fig. S6).

To demonstrate the skin-penetrating properties of MNs, we measured the mechanical strength of blank MNs and mLNP-man-MN. As shown in Fig. 3G, no breakage points were observed for either type of MN even when the force reached the maximum set

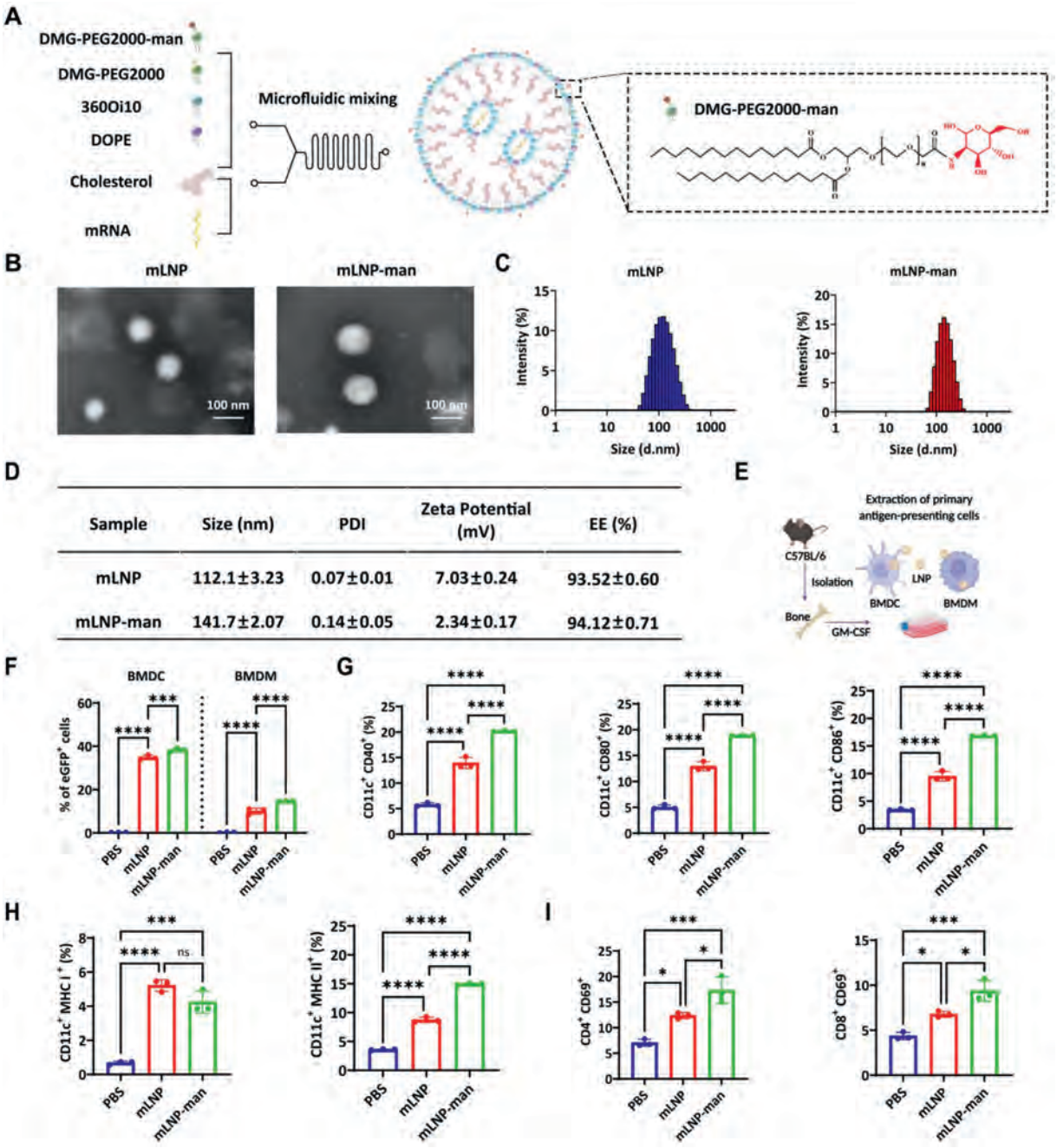


**Figure 2** Preparation and Characterization of mLNP-man. (A) Schematic representation of the preparation of mLNP-man and the structure of DMG-PEG2000-man. (B) Representative TEM images of different LNPs. Scale bar = 100 nm. (C) Hydrodynamic sizes of different LNPs determined by DLS. A representative result is shown. (D) Average sizes, PDI, and zeta potentials of different LNPs determined by DLS. (E) Schematic representation of induction and extraction of BMDCs and BMDMs in C57BL/6 mice. (F) Flow cytometry analysis of the percentage of cells positive for eGFP following transfection with LNPs. (G) Flow cytometry analysis of the ability of the LNPs vaccines to stimulate maturation of BMDCs *in vitro*. (H) Bar graph showing the percentage of $CD11c^+$ MHC $I^+$ and $CD11c^+$ MHC $II^+$ expression on the surface of BMDCs. (I) Bar graph showing the percentage of $CD4^+$ $CD69^+$ and $CD8^+$ $CD69^+$ cells among $CD3^+$ T cells. Data are presented as mean ± SD ($n = 3$). Significance was calculated by one-way ANOVA with a multiple comparisons test (ns, not significant; $^*P < 0.05$, $^{**}P < 0.01$, $^{***}P < 0.001$, $^{****}P < 0.0001$).

value of 70 N. Each microneedle could withstand a compressive force of ≥0.4 N, which significantly exceeds the force required for skin penetration. In addition, it was observed that MNs containing mLNP-man had a smaller displacement than those without mLNP-man under similar stress conditions. This suggests that the incorporation of mLNP-man improved fracture resistance. Next, the skin insertion ability of the mLNP-man-MN was tested in pig skin. Histological images (Fig. 3H) show that the MNs effectively penetrated the epidermis to a depth of approximately 200 μm. Notably, the observed insertion depth was likely smaller than the

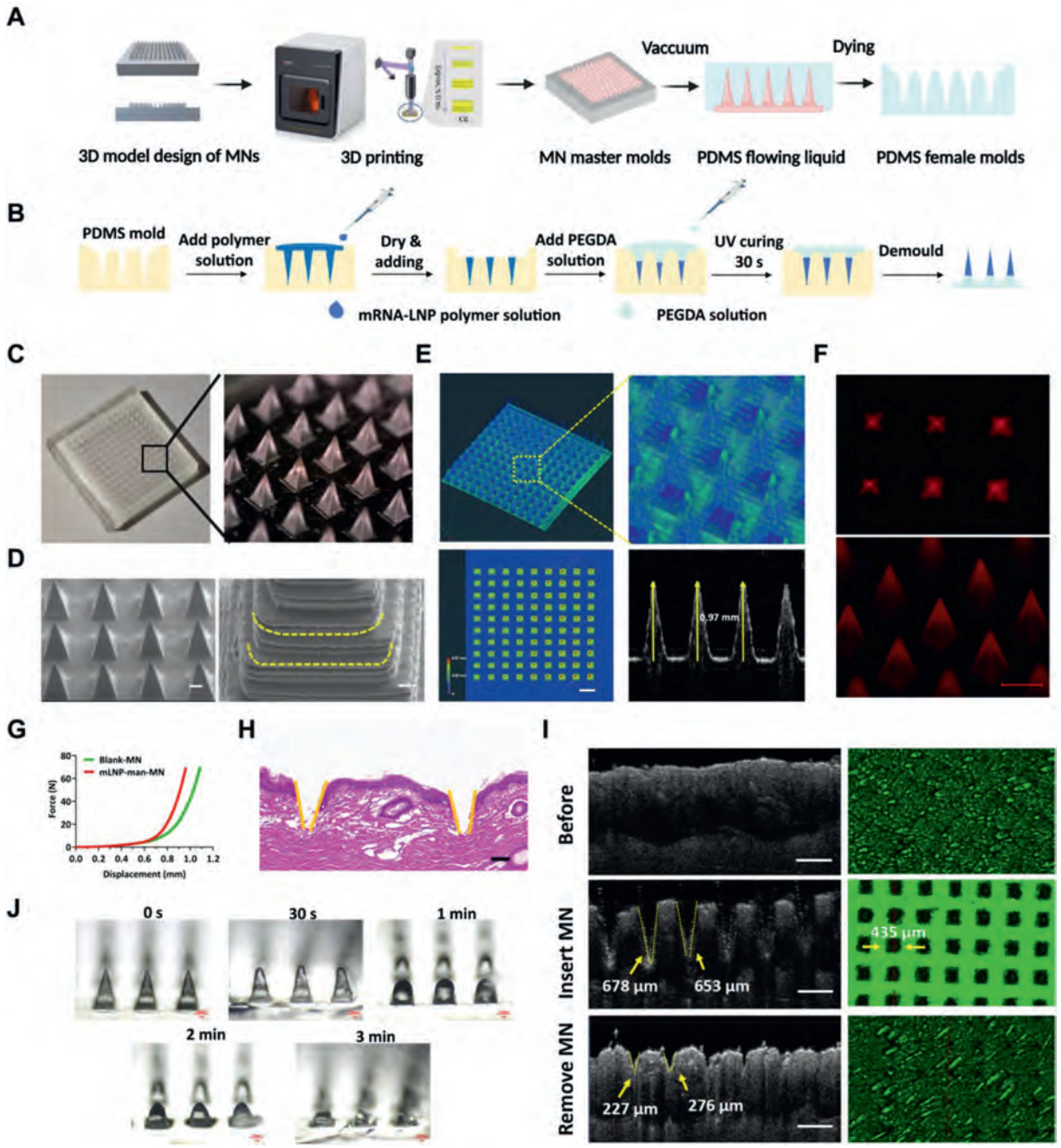


**Figure 3** Fabrication and characterization of mLNP-man-MN. (A) Flowchart for the preparation of MNs master mould and PDMS female moulds. (B) Schematic representation of the mLNP-man-MN preparation process. (C) Stereopic image of mLNP-man-MN. (D) SEM images of mLNP-man-MN. Scale bar of left image = 200 μm. Scale bar of right image = 10 μm. (E) Micro-CT 3D pseudo-colour image of mLNP-man-MN. (F) Fluorescence microscopy images of mLNP-man-MN loaded with DiD-labeled mLNP-man. Scale bar = 200 μm. (G) Mechanical strength of the blank MN and mLNP-man-MN. (H) H&E image of pig skin penetrated by the mLNP-man-MN. Scale bar = 100 μm. (I) OCT images of mLNP-man-MN before and after insertion into pig skin. Upper: OCT image before MN insertion into pigskin; middle: OCT image of MN insertion into pigskin; lower: OCT image of pigskin after MN removal. Scale bar = 500 μm. (J) Dissolution processes of the mLNP-man-MN. Scale bar = 100 μm.

actual insertion depth. This discrepancy can be attributed to factors such as skin tissue rebound, water loss, and dehydration steps during fixation[36]. OCT further confirmed the successful penetration of the MNs. A 435 μm microporosity was clearly visible after application of the MN, and the penetration depth ranged from 600 to 700 μm, and 200−300 μm-deep pores were generated on the skin surface after removal of the MNs (Fig. 3I).

Fig. 3J shows the dissolution of mLNP-man-MNs after their insertion into agarose gel. After the MNs were inserted into a 4% agarose gel, the sharp tips of the MNs disappeared within 30 s and the needle bodies visibly shrunk within 1 min. The needle body layer completely dissolved within 3 min, whereas the backing layer remained relatively intact. This indicates that the drug-loaded layer of mLNP-man-MN can dissolve rapidly within a

short period of time, which is of great significance for the effective internalization of mLNP-man by APCs.

### 3.3. The mRNA-LNPs in MNs showed good stability

To investigate the use of soluble polymers to stabilize LNPs, we compared a variety of biocompatible polymers commonly used for the preparation of soluble microneedles (Supporting Information Fig. S7). The LNPs were mixed with various soluble polymers, dried, and their physicochemical properties and LNP transfection efficiency were determined after re-dissolution. Formulations with mixtures of PVP, Soluplus®, and sucrose were the most effective in stabilizing LNPs (Fig. S7A and S7B). Based on *in vitro* data, it was shown that the stability increased as the polymer-to-mRNA mass ratio increased (Fig. S7C). Finally, we determined the polymer-to-mRNA mass ratio to be 10,000:1. Subsequently, the cytotoxicity and static hemolysis of LNPs in various polymers and MNs were examined separately, and none of the preparations tested impaired cell viability compared to LNPs alone (Supporting Information Fig. S8A). Moreover, no hemolysis occurred in the other sample groups compared to the positive control group, and the hemolysis rate was $<5\%$ in all groups (Fig. S8B).

Next, we tested the stability of LNPs in MNs. The physicochemical properties of LNPs stored at 4 °C for one month (1M) and LNPs extracted from MNs stored at room temperature (25 °C) for two weeks (2W) or at 4 °C for 1M were evaluated respectively. DLS results showed that the particle size and PDI of LNPs in MNs were small, and the particle size and PDI of LNPs in MNs remained almost unchanged after 1M at 4 °C and 2W at 25 °C (Fig. 4A). In contrast, the PDI of LNPs stored at 4 °C for 1M significantly increased ($>0.3$) (Fig. 4B), suggesting that aggregation or fusion of LNPs may have occurred during storage (Fig. 4H). In contrast, the LNPs could redisperse after MN dissolution without irreversibly forming large LNP aggregates. The encapsulation efficiency of each LNP group was determined using a RiboGreen assay. The results showed that the encapsulation efficiency of fresh LNPs and LNPs stored at 4 °C for 1M reached 90% (Fig. 4C) with no significant difference. In contrast, the average encapsulation efficiency of LNPs in MNs and MNs stored at 4 °C for 1M or 25 °C for 2W was significantly lower, maintaining a high level of encapsulation ($>70\%$) despite statistically significant differences.

In addition, we used HEK-293T cells to verify the transfection efficiency of LNPs in MNs. As shown in Fig. 4D, the transfection efficiency of LNPs stored at 4 °C for 1M markedly decreased to 50%. Surprisingly, the transfection efficiency of LNPs in MNs and MNs stored at 4 °C for 1M or 25 °C for 2W were similar to that of fresh LNPs *in vitro*, suggesting that the mRNA molecules were still biologically functionally active. After extracting the mRNA from the LNPs, the stability and integrity of the encapsulated mRNA were studied using gel electrophoresis. MN-encapsulated mRNA (4 °C for 1M or 25 °C for 2W) exhibited intact mRNA bands (Supporting Information Fig. S9). Capillary electrophoresis indicated that there was no significant change in the integrity of the extracted mRNA, with a peak centered at approximately 1500 nucleotides (Fig. 4E). This suggests that the polymer solution not only preserves the structure of LNPs but also does not affect the quality of the mRNA preserved within the LNPs.

To further validate the interactions between LNPs and polymers, as well as their behavior during the MN formation process, we first employed TEM to observe the composite structure of LNPs and polymers. As shown in Fig. 4F, the mixture of PVP and Soluplus® formed a large number of small, uniformly distributed granular structures, which may be due to the self-assembly of the two into nanomicelles. Furthermore, it can be observed that LNPs exhibit a uniform spherical structure (approximately 100 nm) in the mixed solution of PVP and Soluplus®. At the same time, small particles are still present around the LNPs, indicating that the LNPs and Soluplus®/PVP micelles exist independently, with no significant interactions observed. The TEM images of LNPs mixed with Soluplus®/PVP polymers, after curing into MNs and subsequent re-dissolution, reveal that the LNPs retain their intact spherical structure with no significant increase in particle size. A dense population of small particles surrounds the LNPs, and compared to the TEM images of the uncured sample, the number of small particles is markedly increased, with a more compact distribution. Some of these small particles are observed to adhere to the surface of the LNPs. This suggests that during the curing process, as the system transitions from a liquid to a solid state, molecular motion becomes restricted, bringing PVP and Soluplus® micelles closer to the LNPs and increasing the likelihood of interactions. This leads to the aggregation of micelles on the surface of the LNPs (Fig. 4H).

We conducted SEM imaging analysis on the cross-sections of both cured polymer MNs and LNP MNs (Fig. 4G). The SEM images revealed that the surface of the cured polymer MNs exhibited a relatively uniform, continuous, and dense structure. In contrast, the cross-sectional SEM images of the LNPs MNs showed that the LNPs were not fully aggregated but rather dispersed within the continuous matrix or porous network formed by the Soluplus®/PVP polymer. This indicates that the LNPs maintained a certain degree of dispersion during the polymer curing process, without forming large-scale aggregates (Fig. 4H). This structural configuration may enhance the stability and dispersibility of the LNPs, providing a supportive environment for their uniform distribution within the polymer matrix.

### 3.4. The mLNP-man-MN vaccines recruited APCs and activated draining lymph nodes (dLNs)

We investigated whether the MN vaccines induced innate immune responses. At 1−14 days post-MN immunization, we collected dorsal skin from the application site to evaluate the dynamic changes in APCs at the application site. Although no significant differences were observed among the groups on Day 1 (Fig. 5A), mLNP-man was better taken up and expressed by APCs in the skin (Fig. 5B), which aligns with the results of the *in vitro* uptake and expression in BMDCs and BMDMs (Fig. 2F). Seven days after MN immunization, the proportion of $CD11c^+$ $CD80^+$ and $CD11b^+$ $F4/80^+$ cells in the mLNP and mLNP-man vaccine groups showed an increasing trend, and the mLNP-man group exhibited more significant immune activation characteristics than the mLNP vaccine group (Fig. 5A). This suggests that mLNP-man effectively targeted APCs and promoted their maturation compared with unmodified mLNP. Fourteen days after MN immunization, APC levels induced by both mLNP and mLNP-man vaccines returned to baseline levels. The mLNP-man vaccines rapidly recruited and activated APCs while avoiding continuous immune activation, which can cause adverse immune responses. Similarly, APCs at the site of mLNP-man-IM immunization showed the same dynamic trend, and MN immunization seemed to be more effective in triggering the recruitment and activation of APCs than IM immunization (Supporting Information Fig. S10).

To visually evaluate antigen drainage into the inguinal lymph nodes of mice after vaccine immunization in different groups, the inguinal lymph nodes of mice were removed 24 h after

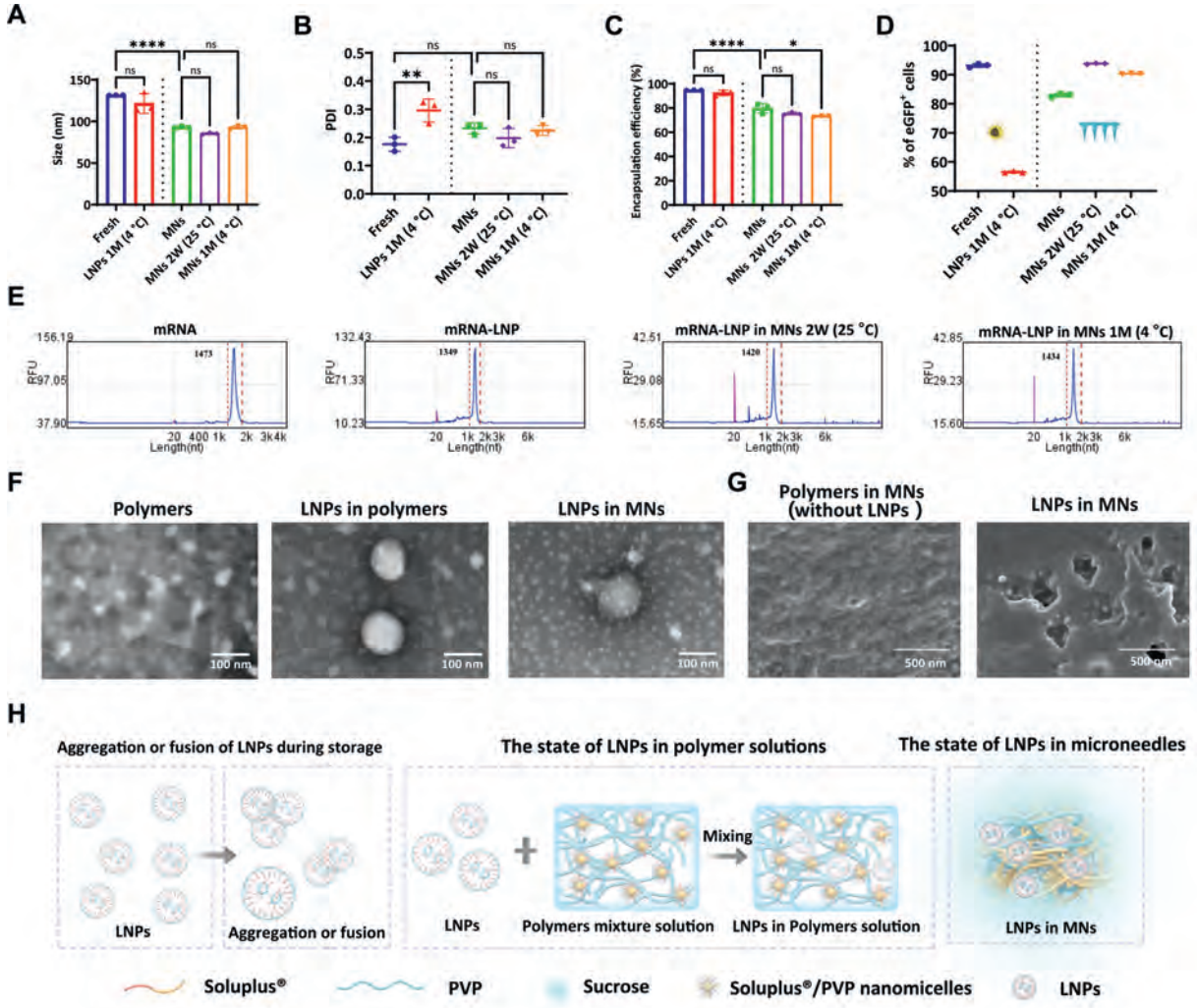


**Figure 4** Stability characterization of mRNA-LNPs in MNs. (A) Particle size, (B) PDI, and (C) encapsulation efficiency of fresh LNPs, LNPs stored for 1M (4 °C), LNPs in MNs stored for 2W (25 °C), as well as LNPs in MNs stored for 1M (4 °C). (D) Transfection efficiency of fresh LNPs, LNPs stored for 1M (4 °C), LNPs in MNs stored for 2W (25 °C), as well as LNPs in MNs stored for 1M (4 °C) in HEK-293T cells. (E) Analysis of mRNA fragments in fresh LNPs, MNs stored for 2W (25 °C), and MNs stored for 1M (4 °C) using capillary electrophoresis. (F) TEM images of polymers, LNPs in polymers (liquid state), LNPs in MNs. Scale bar = 100 nm. (G) SEM images of the cross-sections of polymer MNs (without LNPs) and LNPs MNs. Scale bar = 500 nm. (H) Schematic representation of aggregation and fusion of LNPs during storage and stabilization of LNPs in polymers. Data are presented as mean ± SD ($n = 3$). Significance was calculated by one-way ANOVA with a multiple comparisons test (ns, not significant; $^{*}P < 0.05$, $^{**}P < 0.01$, $^{***}P < 0.001$, $^{****}P < 0.0001$). M, month; W, week.

immunization, fluorescently stained, and scanned for imaging. The fluorescence images showed that (Fig. 5C) the expression of green eGFP was clearly observed in the mLNP-man-MN and mLNP-man-IM groups, which was mainly concentrated in the cortical region of the lymph nodes. It was demonstrated that after mLNP-man-MN immunization, APCs in the skin could efficiently take up LNPs and express target proteins, thus draining into the lymph nodes. This result was consistent with the flow cytometry results of the draining lymph nodes 24 h after MN immunization with DiD-mLNPs and DiD-mLNP-man (Supporting Information Fig. S11).

Furthermore, we collected lymph nodes from mice 7 days after immunization to analyze the maturation level of homing DCs (Supporting Information Fig. S12). The results of this study showed an increase in the expression of $CD80^{+}$ $CD86^{+}$ in DCs in the mLNP-man-MN group after immunization, which was significantly different from that in the mLNP-man-IM group (Fig. 5D). The mLNP-man-MN vaccines promoted the activation of lymph node APCs, which in turn induced an adaptive immune response. The level of lymph node T cell activation was further examined. The results showed that the expression of $CD69^{+}$ in $CD3^{+}$ T cells in the lymph nodes of mice in the mLNP-man-MN vaccine group was significantly elevated (Fig. 5E), suggesting that T cell activation was enhanced by MN immunization, which was significantly different from that induced by IM immunization.

### *3.5. The mLNP-man-MN vaccines induced an effective humoral immune response*

Next, we evaluated the immune responses of BALB/c mice vaccinated with mLNP or mLNP-man *via* the IM and MN routes.

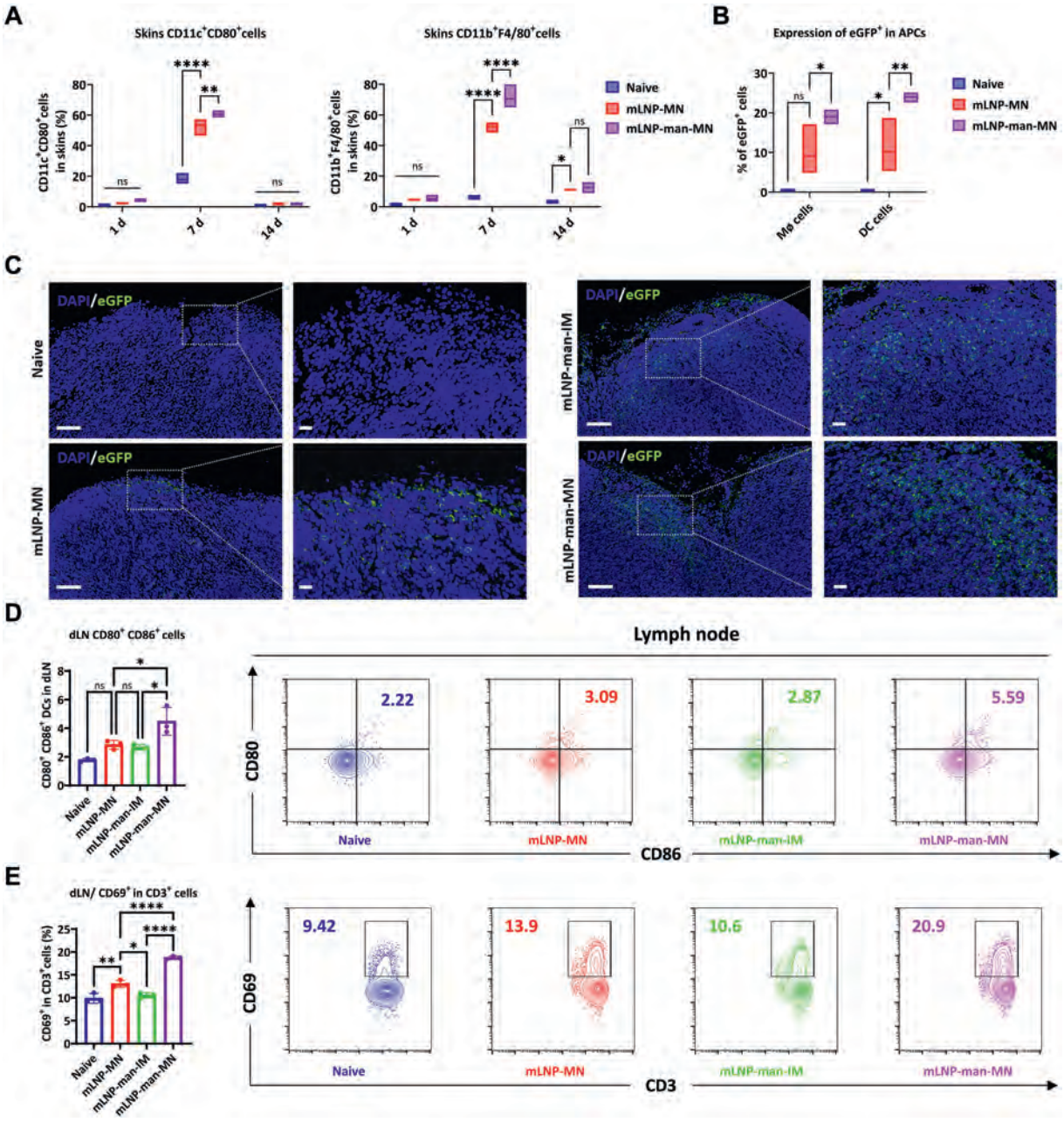


**Figure 5** mLNP-man recruited APCs and activated dLNs after MN immunization. (A) Box plot showing the number of $CD11c^+$ $CD80^+$ (left), $F4/80^+$ $CD11b^+$ (right) cells at the site of administration in mice 1−14 days after MN immunisation. (B) Expression of $eGFP^+$ in APCs at the site of administration. (C) Immunofluorescence of LNPs draining into lymph nodes and expressing $eGFP^+$ 24 h after IM or MN immunisation. Scale bar of left images = 100 μm. Scale bar of right images = 20 μm. (D) Left, bar graph showing the proportion of $CD80^+$ $CD86^+$ cells among $CD11c^+$ lymph node cells. Right, Representative flow cytometry contour plots of DCs maturation ($CD80^+$ $CD86^+$) in lymph nodes of BALB/c mice immunized for 7 days. (E) Left, Bar graph showing frequency of $CD3^+$ $CD69^+$ cells in lymph node cells. Right, Representative flow cytometry contour plots of T-cell activation ($CD3^+$ $CD69^+$) in lymph nodes 7 days of BALB/c mice immunized for 7 days. Data are presented as mean ± SD ($n = 3$). Significance was calculated by one-way ANOVA with a multiple comparisons test (ns, not significant; $^*P < 0.05$, $^{**}P < 0.01$, $^{***}P < 0.001$, $^{****}P < 0.0001$).

A schematic of the immunization modality and cycle detection procedure is shown in Fig. 6A. The titers of IgG antibodies specific to the RBD were assayed on Days 21 and 42 post-immunization. The results showed that mLNP-man-MN immunization effectively induced RBD-specific IgG antibodies on Days 21 and 42 (Fig. 6B and C), with no significant difference compared to the mLNP-man-IM group. After enhanced immunization, the antibody levels further increased, and the RBD-specific IgG antibody levels induced by the mLNP-man-MN group were significantly higher than those induced by the mLNP-MN group (Fig. 6C).

Serum titers of RBD-specific IgG1 and IgG2a were measured 42 days after initial immunization to assess the immune bias of the vaccine-induced antibody response. The antigen-specific IgG1 titers in the mLNP-MN and mLNP-man-MN groups were

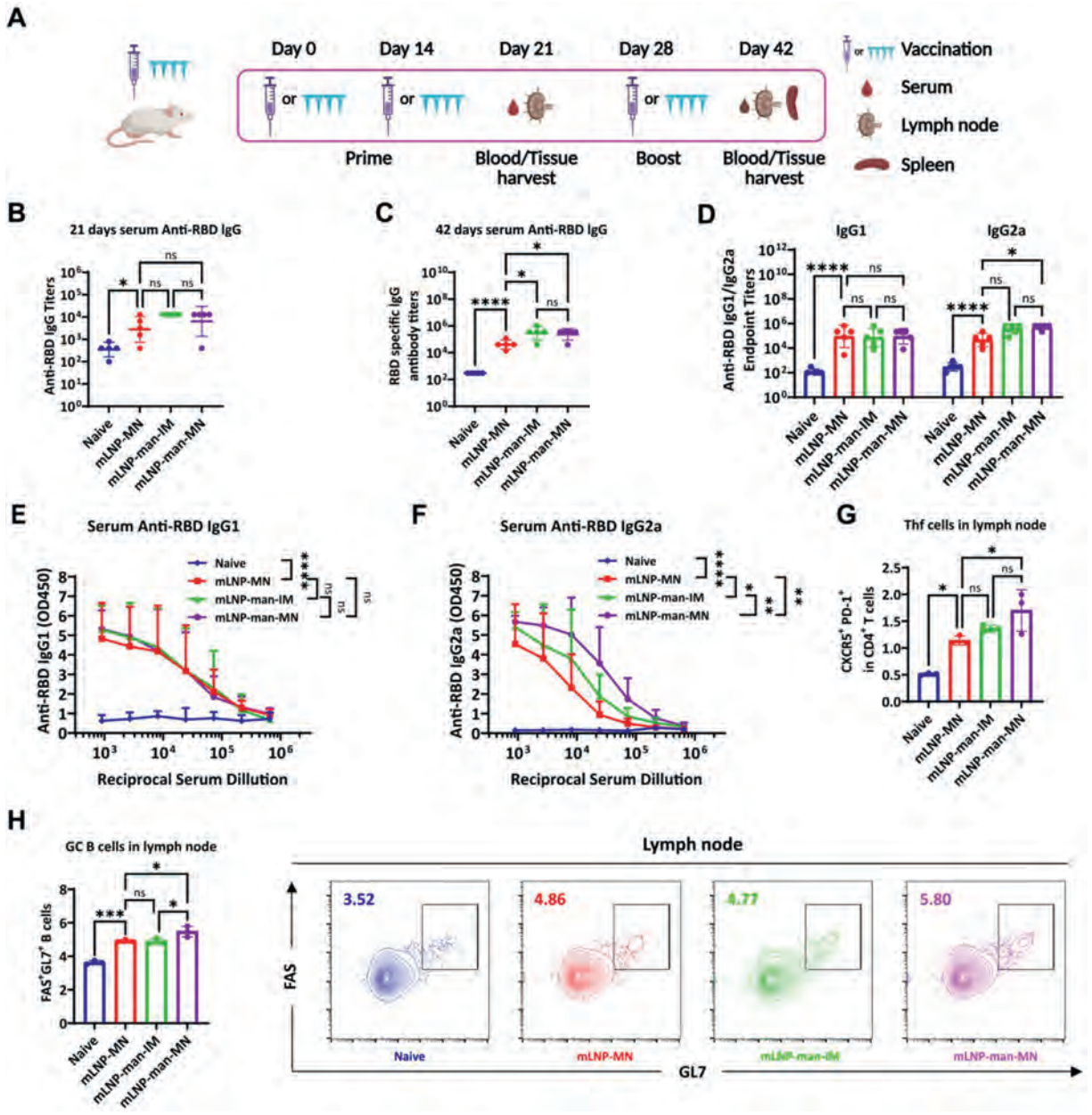


**Figure 6** The mLNP-man-MN vaccines induces robust RBD-specific antibody responses in mice. (A) Schematic diagram of animal immunisation. (B, C) On Days 21 and 42, IgG titres in mouse serum were determined by ELISA. (D) RBD-specific IgG2a versus IgG1 endpoint serum titres were measured on Day 42. (E) RBD protein-specific IgG1 titre and (F) IgG2a titre in serum of mice after 42 days of immunisation. Data are presented as mean ± SD ($n = 5$). (G) Bar graph showing the frequency of lymph node Thf cells after 21 days of MN or IM immunisation. Data are presented as mean ± SD ($n = 3$). (H) Left, bar graph showing the frequency of lymph node $FAS^+$ $GL7^+$ cells. Right, representative flow cytometry contours of lymph node $FAS^+$ $GL7^+$ cells after 21 days of MN or IM immunisation. Data are presented as mean ± SD ($n = 3$). Two-way mixed ANOVA followed by Holm-Sida' k test for treatment effect was used in (E) and (F). One-way ANOVA and Tukey's test between groups for other pictures (ns, not significant; $*P < 0.05$, $**P < 0.01$, $***P < 0.001$, $****P < 0.0001$).

comparable to those in the mLNP-man-IM group (Fig. 6D and E), suggesting that the route of immunization and the vaccine vehicle had no significant effect on the RBD-specific IgG1 titers. In contrast, mice in the mLNP-man-MN group had higher IgG2a antibody titers than those in the mLNP-MN group, whereas there was no significant difference when compared with the mLNP-man-IM group (Fig. 6D and F). This suggests that vaccine carriers can influence the immunological bias of antibody responses. In summary, mLNP-man-MNs increased the virus-specific Th1-associated IgG2a response, which is consistent with previous reports showing that mannose-modified LNPs enhance antigen-specific Th1 responses[37].

Next, we assessed the induction of follicular helper T cells (Tfh cells) and germinal center B (GCB) cells after IM or MN immunization. Tfh cells are a subpopulation of CD4-positive helper T cells involved in the humoral response and trigger the

differentiation of GC B cells into antibody-secreting plasma and memory B cells (Supporting Information Fig. S13). In addition, the GC response is the basis for the induction of high-quality and long-lasting B-cell responses[38]. We collected lymph nodes from mice immunized for 21 days and obtained and quantified Tfh and GC B cells in the LNs using flow cytometry. The results showed that the proportion of Tfh cells increased approximately 3-fold after immunization with mLNP-man-MN compared to that in the mLNP MNs group (Fig. 6G). Similarly, mLNP-man-MNs promoted the production of GC B ($CD19^+$ $FAS^+$ $GL7^+$), which was significantly different from that in the mLNP-man-IM and mLNP-MN groups (Fig. 6H). In conclusion, mLNP-man-MNs effectively promoted the production of Tfh and GC B cells *in vivo*, which is essential for enhancing humoral immunity.

### *3.6. The mLNP-man-MN vaccines elicited memory T-cell responses in mice*

To assess the ability of mLNP-man-MNs to induce immune memory and stimulate immune responses *in vivo*, we collected the spleens of mice on Day 42 to prepare single-cell suspensions and determined the proliferation level of splenocytes using the CCK8 method. Splenocytes in all the experimental groups showed different degrees of proliferation. The proliferation index of splenocytes in the mLNP-man-MN group was not significantly different from that in the mLNP-man-IM group but was significantly higher than that in the mLNP-MN group, which indicated that mLNP-man had a better effect on immune memory (Fig. 7A).

Central memory T cells (TCM) play a crucial role in the memory response of the immune system. They survive for prolonged periods in the immune system, proliferate rapidly, and exert effector functions upon re-encountering specific antigens[39]. Forty-two days after immunization, we evaluated the levels of TCMs in the secondary lymphoid organs (lymph nodes and spleen) of mice from different groups. The results showed that both mLNP-man-MN and mLNP-man-IM groups significantly induced higher levels of $CD4^+$ TCMs and $CD8^+$ TCMs in the lymph nodes, and these levels were significantly higher than those in the mLNP-MN group (Fig. 7B and Supporting Information Fig. S14). Compared with the naive group, the mLNP-MN group also effectively promoted the generation of TCMs in the lymph nodes (an increase of approximately 1%), thereby effectively enhancing systemic immune memory. Similarly, mLNP-man-MN promoted the generation of $CD4^+$ TCMs (approximately 2.73%) and $CD8^+$ TCMs (approximately 1.80%) in the spleen, which was higher than that in the mLNP-man-IM and mLNP-man-MN groups (Fig. 7C and Fig. S14). This suggests that mLNP-man-MNs can more effectively induce memory T cell responses, enhance immune memory function, and provide better immune protection against pathogen reinfection.

In addition, several studies have shown the interactions in the migration of T cells from the skin to other distal mucosal tissues, especially in the homing of $CD8^+$ T cells from the skin to the lungs[25,40,41]. To assess the cellular immune response in the lungs of immunized mice, lung tissues were collected and digested to isolate individual cells for staining and flow cytometry analysis at 42 days post-immunization. High CD44 expression is typically associated with memory and activated T-cells. Notably, MN immunization effectively induced the formation of $CD44^+$ phenotypic memory T cells in the lungs of mice (Fig. 7D and Fig. S14), with significant differences compared to the muscle-immunized mice. These results suggest that mLNP-man-MNs, the immune response in the lungs can be effectively activated to induce the activation and differentiation of T cells with memory properties, which can respond rapidly to reinfection, provide rapid immune protection, and reduce the transmission and replication of the virus. The above findings emphasize the potential of mLNP-man-MN vaccines in promoting the formation of memory T cells in secondary lymphoid organs and lung tissues and provide an important strategic direction for the long-term maintenance and enhancement of immune memory.

### *3.7. The mLNP-man-MN vaccines induced T cell cytokines in splenocytes and lung cells*

To further evaluate the cellular immune response induced by the mLNP-man-MN vaccines in mice, we performed ELISpot and ICS assays. The secretion of IFN-$\gamma$ and IL-4 in mice splenocytes was measured using an ELISpot assay 42 days after immunization. Significantly, the mLNP-man-MN group induced significantly higher levels of splenic IFN-$\gamma^+$ T cells than the other groups, with approximately 500 spot-forming units (SFUs) induced per $5 \times 10^5$ splenocytes (Fig. 7E and F). Both mLNP-man-MN and mLNP-man-IM induced a higher frequency of splenic IL-$4^+$ T cell responses (approximately 100 SFUs), whereas the number of splenic IL-$4^+$ T cell response SFUs in the mLNP-MN group was less than 10 and could be considered negligible (Fig. 7E and G).

To evaluate the cellular immunity induced in local mucosal tissues, an IFN-$\gamma$ ELISpot assay was also conducted on lung lymphocytes. We found that on Day 42, mLNP-man-IM immunization failed to induce significant IFN-$\gamma^+$ T-cell responses in the lungs, which were not significantly different from the results in controls (Fig. 7H and I). Notably, the mLNP-man-MN group induced approximately 10 SFUs per $2 \times 10^5$ lung lymphocytes, whereas almost no SFUs were observed in the mLNP-man-IM group (Fig. 7H and I). These results indicate that delivery of the mLNP-man vaccine to the skin *via* MNs is more effective in inducing lung-resident antigen-specific T-cell responses than the conventional IM immunization route. Despite the relatively low T-cell responses, this strategy provides an essential strategic avenue for developing vaccines against respiratory viral diseases.

In addition, splenocyte samples from BALB/c mice immunized for 42 days were collected, peptide library-stimulated for intracellular factor staining, and analyzed using flow cytometry for levels of IFN-$\gamma$, TNF-$\alpha$, IL-2, and IL-4 induced by different immunization modalities. Compared with the mLNP-MN group, mLNP-man-MN significantly increased the release of IFN-$\gamma$, IL-2, and TNF-$\alpha$ cytokines from RBD-specific $CD8^+$ T cells (Fig. 7K−M). Similar results were observed for the $CD4^+$ T-cell subset (Supporting Information Fig. S15). Further analysis also showed (Fig. 7J) that the frequency of multifunctional $CD8^+$ T cells simultaneously expressing IFN-$\gamma$, IL-2, and TNF-$\alpha$ was higher in the mLNP-man-MN group than in the mLNP-man-IM group. In contrast, IL-4 levels were significantly lower than those of IFN-$\gamma$ (Fig. 7N and Fig. S15), suggesting the predominance of Th1-type immune responses. These results are consistent with those of the ELISpot assay.

The safety of BABL/c mice immunized using different modes of immunization was assessed one month after the last immunization. No pathological abnormalities were observed in the major organs of mice in any of the groups (Supporting Information

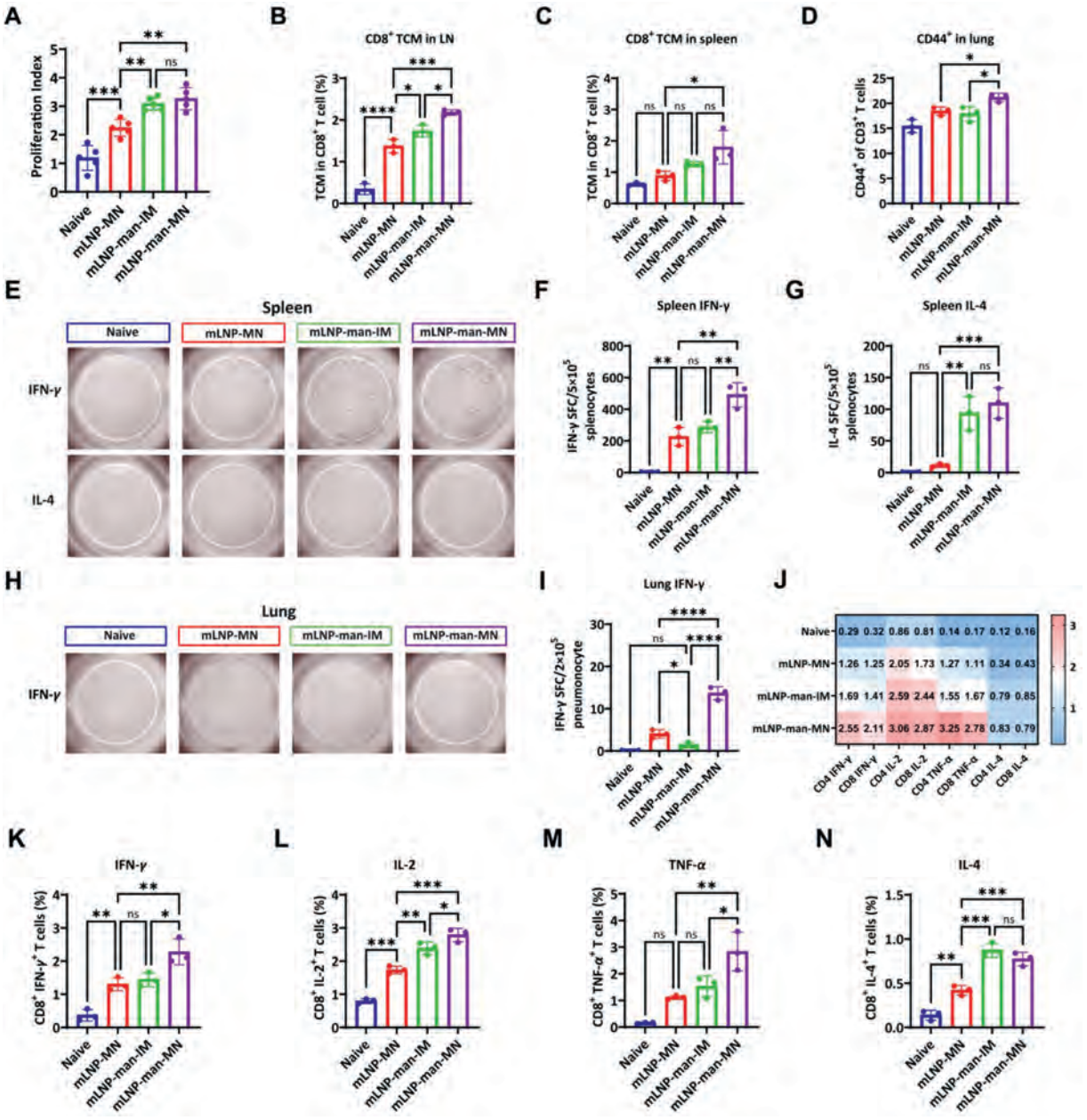


**Figure 7** The mLNP-man-MN vaccines induces stronger multifunctional T cell responses. (A) Proliferation of splenocytes after antigenic stimulation *ex vivo* using the CCK-8 kit. Data are presented as mean ± SD ($n = 5$). (B) Bar graphs show frequencies of $CD8^+$ TCM cells in lymph nodes and (C) $CD8^+$ TCM in spleen. (D) Bar graph showing the frequency of $CD3^+$ $CD44^+$ cells in lungs. (E) Antigen-specific IFN-γ (top) and IL-4 (bottom) ELISpot assays were performed using spleen lymphocytes isolated on Day 42 at $5 \times 10^5$ spleen cells per well. (F) Quantitative bar graph of SFCs producing IFN-γ and (G) IL-4 from splenocytes. (H) Quantitative bar graph of SFCs production of IFN-γ by lung cells. (I) Results of IFN-γ ELISpot assay of lung lymphocytes from mice after Day 42 of immunisation, $2 \times 10^5$ lung cells per well. (J) Following stimulation of the RBD peptide pool, the multifunctional T cell response in the spleen was visualised using a heat map on Day 42 post-immunisation. (K−N) Bar graph of the proportion of RBD-specific IFN-$\gamma^+$, TNF-$\alpha^+$, IL-$2^+$ or IL-$4^+$ $CD8^+$ T cells cells in spleens on Day 42 after immunisation. Data are presented as mean ± SD ($n = 3$). Groups were compared by one-way ANOVA and Tukey's test (ns, not significant; *$P < 0.05$, **$P < 0.01$, ***$P < 0.001$, ****$P < 0.0001$).

Fig. S16). And blood biochemical indices remained within the normal reference ranges (Supporting Information Fig. S17). Furthermore, a gradual increase in body weight was noted in all groups of mice following MN or intramuscular immunization, indicating that the mLNP-man-MN vaccine had an excellent safety profile (Supporting Information Fig. S18).

### *3.8. The mLNP-man-MN vaccines had a certain clearance effect on pulmonary pseudoviruses*

To further verify whether MN-mediated immunization with mLNP-man protects against viral attack on the lungs, we immunized H11-K18-hACE2 transgenic mice using the same

method and performed a SARS-CoV-2(D614G)-GFP-Luc pseudoviral lung attack (Fig. 8A). Two days after infection, the mice were euthanized, and lung samples were collected. The results of *in vitro* fluorescence imaging and immunofluorescence staining of the lungs showed a larger area of pseudovirus infection and higher GFP fluorescence intensity in the naive and IM groups. However, the mLNP-man-MN group showed a relatively low viral infection rate (Fig. 8B−D), suggesting that the vaccine had a protective effect. Flow cytometry analysis of the proportion of GFP-positive cells yielded results similar to those of *ex vivo* imaging of the lung tissue (Fig. 8E). This suggests that the MN-mediated mLNP-man immunity protects against viral attacks in the lungs to a certain extent.

Next, we evaluated the neutralization potential of serum against the SARS-CoV-2(D614G)-GFP-Luc pseudovirus. At 42 days post-immunization, mouse sera were diluted 1:100 for neutralization efficiency assessment (Fig. 8G). Serum samples from the PBS group showed no inhibitory effect on the entry of SARS-CoV-2 D614G pseudovirus into cells expressing ACE2 receptors. In contrast, sera from mLNP-man-IM and mLNP-man-MN vaccine-immunized mice exhibited significant neutralizing activity against SARS-CoV-2 D614G pseudoviruses, with no significant difference between the two groups (Fig. 8F).

## 4. Discussion

In this study, we constructed an mRNA-LNP MN vaccine system that successfully solidified LNPs in MN matrix materials without affecting their physicochemical properties or transfection efficiency. The physicochemical properties and biological activities of the mRNA-LNP complexes remained stable after storage at 25 °C for 2W or 4 °C for 1M, thus enhancing the convenience of the vaccine in terms of transportation, storage, and use. The matrix material for the MNs was formulated using a blend of PVP, Soluplus®, and sucrose. Sucrose is known to be highly advantageous for maintaining the stability of LNPs. PVP, which is known for its excellent biocompatibility, is widely used in the pharmaceutical and cosmetic industries. They also provide good mechanical strength in the dry state, ensuring that the MNs can effectively penetrate the skin. In addition, the hydrophilic polymer PVP acts as a stabilizing agent that creates a site-blocking effect on the particle surface, ensuring effective repulsion between the nanoparticles, and thus inhibiting particle growth[42]. A recent study also showed that MNs loaded with mRNA-LNPs prepared using PVP and polyvinyl alcohol polymer materials can remain shelf-stable at room temperature for at least six months[21]. This indicates that PVP-based MNs are ideal for mRNA delivery.

Furthermore, Soluplus® is a graft copolymer with a hydrophilic polyethylene glycol (PEG) backbone and hydrophobic vinyl caprolactam/vinyl acetate side chains[43,44]. In aqueous solutions, Soluplus® self-assembles into nano micelles, with the hydrophobic segments (polyvinyl acetate and polycaprolactone) forming the micelle core and the hydrophilic segments (polyvinyl alcohol) forming the shell. When LNPs are dispersed in a Soluplus®/PVP polymer solution, the LNPs and Soluplus®/PVP micelles exist independently, with no significant interactions observed. It is hypothesized that the surface charges of the LNPs and micelles or the steric hindrance effect of the PVP polymer chains may prevent direct interactions between them, thereby further inhibiting LNP aggregation[45,46]. Simultaneously, under liquid conditions, the solvent provides sufficient dispersive force, allowing the LNPs and micelles to remain independently dispersed.

During the curing process, as the system transitions from a liquid to a solid state, molecular motion becomes restricted. The distance between PVP, Soluplus® micelles, and LNPs gradually decreases, and interactions such as electrostatic forces, hydrogen bonding, and van der Waals forces may lead to the aggregation of micelles on the surface of LNPs[47,48]. This results in a more compact distribution of micelles around the LNPs. Additionally, Soluplus®/PVP micelles may undergo fusion or rearrangement during the curing process, forming a continuous polymer matrix or porous structure. The hydrophilicity of PVP promotes the formation of a physically cross-linked network, which not only provides a stable dispersion environment for the LNPs but also effectively prevents LNP aggregation through steric hindrance effects[42]. The LNPs are relatively dispersed within the continuous matrix or porous network formed by the Soluplus®/PVP polymer. This structural configuration is likely to enhance the stability and dispersibility of the LNPs. In summary, the combination of sucrose, Soluplus®, and PVP produced a synergistic effect, further enhancing the stability of LNPs (Fig. 4H).

Although we extensively evaluated the stability of the mRNA-LNP MN vaccine from various perspectives, further in-depth exploration of its complex stabilization mechanism and comprehensive quality control system is required. On the one hand, it is necessary to design a more comprehensive and systematic stability assessment program to investigate the dynamic changes in the physicochemical properties and bioactivity of LNPs under long-term storage conditions; on the other hand, it is necessary to validate their bioactivity in complex physiological environments in animals to ensure the reliability and robustness of this technology when it is transferred from the laboratory to clinical practice or large-scale application.

MNs can directly target many APCs, thereby inducing a robust immune response. To enhance the APC targeting of the LNPs, we optimized the LNP formulation by modifying it with mannose. Based on the recruitment of APCs to the skin, mLNP-man can target a large number of APCs and facilitate their migration to the lymph nodes, promoting the maturation of APCs and upregulating the expression of costimulatory molecules, including CD80 and CD86. Mature APCs trigger specific $CD4^+$ and $CD8^+$ T cells. On the one hand, $CD4^+$ T cells can differentiate into Tfh cells (Fig. 6G), which interact with GC B cells (Fig. 6H) to differentiate into plasma cells to produce specific antibodies and provide protective immunity (Fig. 7B and C); on the other hand, $CD8^+$ T cells can directly kill virus-infected cells and provide protective immunity. Activated T cells enter the spleen through blood circulation. Upon restimulation with antigen, the resident activated T cells in the spleen rapidly secrete various cytokines such as IFN-$\gamma$, IL-2, and TNF-$\alpha$, thereby triggering a multifaceted cellular immune response (Fig. 7J). Therefore, the integration of mannose-modified LNPs with polymer MNs has great potential for enhancing vaccination effectiveness. However, in the absence of this integration, we observed a significantly diminished immune response when either mLNP-man or mLNP-MN alone was administered *via* IM injection. Furthermore, the mLNP-man-MN vaccination strategy effectively induces durable humoral and cellular immune responses (Supporting Information Fig. S19), providing critical evidence for the long-term protective efficacy of the vaccine.

Since SARS-CoV-2 is a respiratory virus, we also evaluated the pulmonary cellular immune response induced by MN or IM

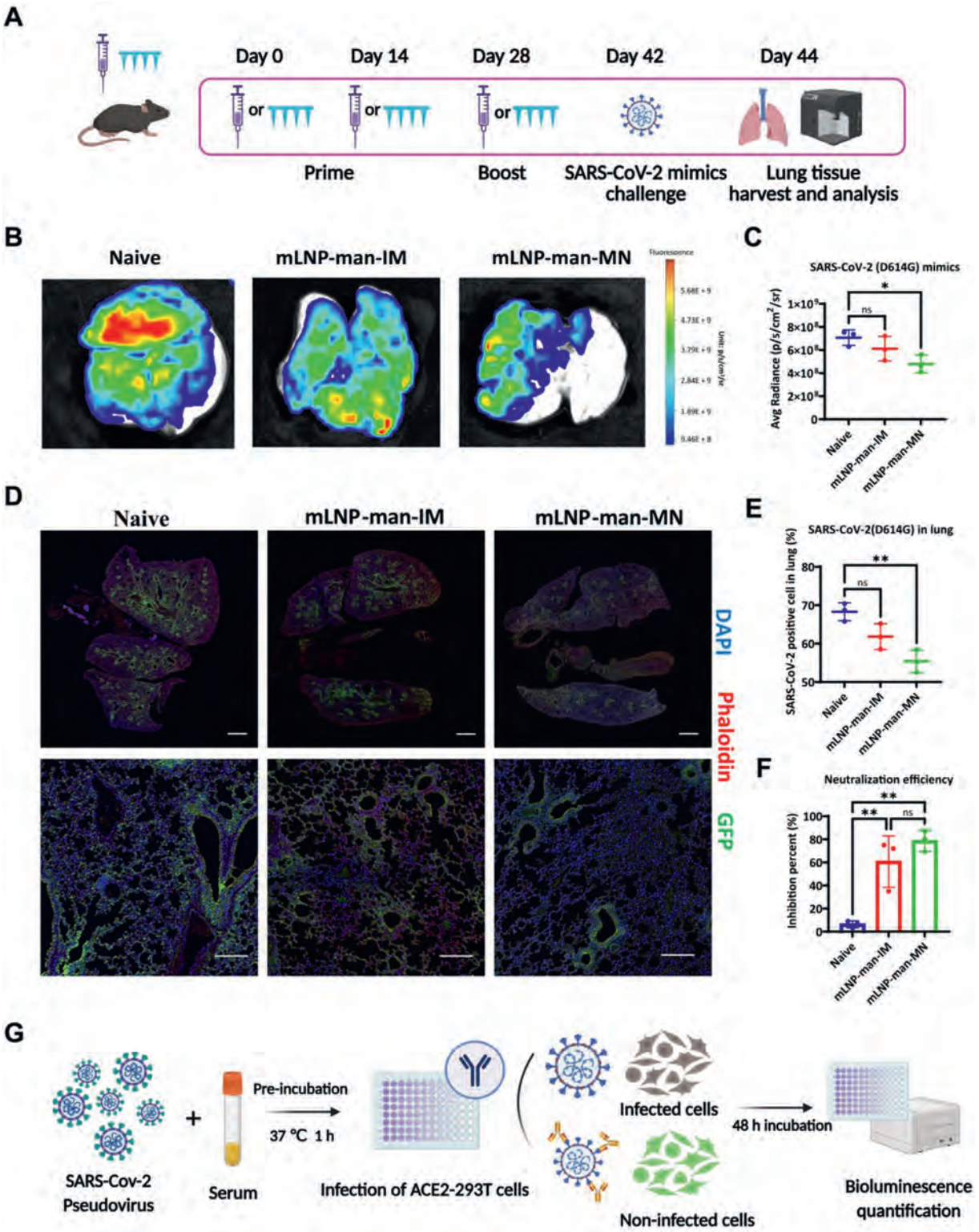


**Figure 8** H11-K18-hACE2 mice pseudovirus attack challenge. (A) Schematic diagram of immunization and pseudovirus challenge experiments in H11-K18-hACE2 mice. (B) *Ex vivo* imaging of lung tissue on Day 2 after the pseudovirus attacked the lung tissue to detect the average fluorescence intensity of GFP ( $\times 10^3$ p/s/cm$^2$/sr). (C) Quantification of GFP fluorescence intensity in mouse lung tissue. (D) Immunostaining imaging of the lung tissue. Scale bar of top images = 2 mm. Scale bar of bottom images = 200 μm. (E) Verification of GFP-positive expression rate in mouse lung cells in each group by flow cytometry. (F) Neutralisation efficiency of mouse serum at a dilution of 1:100 against SARS-CoV-2 D614G pseudovirus on Day 42 of immunisation. Data are presented as mean ± SD ($n = 3$). (G) Schematic of the detection principle of SARS-CoV-2 D614G pseudovirus neutralization. Groups were compared by one-way ANOVA and Tukey's test (ns, not significant; $*P < 0.05$, $**P < 0.01$, $***P < 0.001$, $****P < 0.0001$).

vaccination. Notably, we found that MN-mediated mLNP-man induced the formation of CD44 phenotype memory T cells in the lungs (Fig. 7D) and produced an increase in IFN-$\gamma$ levels (Fig. 7H and I). Although the amount was not substantial, it showed a significant difference compared to IM vaccination. In addition, in lung attack experiments in H11-K18-hACE2 transgenic mice, mLNP-man-MN-immunized mice had a relatively low rate of lung virus infection compared to the naive and mLNP-man-IM groups. This suggests that the generated lung memory T cells were able to protect against lung attack by SARS-CoV-2 D614G pseudovirus (Fig. 8)[29,30,49,50]. This result was also confirmed in a study by Liu et al.[25], in which skin infection with a vaccine strain generated tissue-resident memory T cells in the lungs, providing significant protection against lethal pulmonary challenge by the vaccine strain even in the absence of antibodies and circulating T cells.

Increasing evidence suggests that the anatomical site of initial T-cell activation does not always predict subsequent tissue-specific homing. The crosstalk between T cells primed in the skin and their migration to other distant mucosal tissues has been well documented[26,41,51,52]; however, the mechanisms by which antigen-specific $CD8^+$ T cells disseminate and acquire residency in epithelial barrier tissues far from the site of immunization remain unclear. One paradigm suggests that early effector $CD8^+$ T cell subsets acquire additional homing potential through migration to distant LN microenvironments[53−55]. A recent study found that microneedle array-mediated immunization targeting the epidermis and stimulating predominantly Langerhans cells resulted in an increase in the expression of the $\alpha 4\beta 1$ adhesion molecule on the surface of $CD8^+$ T cells[40]. This might play a role in the homing of T cells to the lungs. Thus, MN immunization appears to be a promising strategy for inducing protective systemic and pulmonary T-cell immunity. Nevertheless, the present study demonstrated that MN-mediated immunization resulted in the expression of CD44 on lung T cells and a limited level of IFN-$\gamma$ secretion. This suggests that MN-mediated immunization does not elicit a robust T cell response in the lungs, similar to skin scarring or pulmonary mucosal administration. In the future, it may be beneficial to consider the addition of adjuvants or a combination of MN immunization with pulmonary mucosal immunization with the aim of enhancing both systemic and mucosal responses. Given the advantages of mLNP-man-MN vaccines in mucosal immune induction, further studies and validation of the interactions between MN cutaneous and pulmonary immunity will provide a more profound scientific basis and strategy for designing respiratory virus vaccines. In addition, the validation of the versatility and flexibility of this vaccine platform in different disease models will advance its application in the field of infectious diseases.

## 5. Conclusions

We constructed a novel and stable mRNA-LNP MN vaccine delivery system. The physicochemical properties and biological activity of the mRNA-LNP complexes were maintained after storage at 25 °C for 2 weeks or at 4 °C for 1 month. Compared to traditional IM immunization, MN immunization is superior in inducing systemic humoral immunity as well as inducing T-cell responses in the spleen and lungs. This study provides a new strategy for further development of mRNA vaccines against a wide range of infectious pathogens, which will help improve vaccine accessibility and efficacy on a global scale.

## Acknowledgments

This study was supported by the National Key Research and Development Program of China (No. 2023YFC2605000, China). We appreciate the help of Shanshan Yang (Hangzhou Dianzi University, Automation College, Hangzhou, Zhejiang, China) in the use of Micro-CT instrument and its data processing.

## Author contributions

Xiaoxuan Hong, Chunying Cui, and Aiping Zheng conceived and designed the experiments; Zengming Wang performed experiments and reviewed the manuscript; Xiaolu Han, Yi Cheng, Nan Liu, Haonan Xing and Xiwei Wang analyzed the data; Jinghu Lou, Yue Li and Jintao Lin performed *in vivo* experiments; Xiaoxuan Hong and Xianfu Li were involved in writing the manuscript; Hui Zhang and Shuang Zhang edited the language. All authors critically reviewed and approved the final version.

## Conflicts of interest

The authors have no conflicts of interest to declare.

## Appendix A. Supporting information

Supporting information to this article can be found online at https://doi.org/10.1016/j.apsb.2025.10.006.

## References

1. Miao GG, Chen ZQ, Cao HS, Wu WH, Chu X, Liu HY, et al. From immunogen to COVID-19 vaccines: prospects for the post-pandemic era. *Biomed Pharmacother* 2023;**158**:114208.
2. Morrison H, Jackson S, McShane H. Controlled human infection models in COVID-19 and tuberculosis: current progress and future challenges. *Front Immunol* 2023;**14**:1211388.
3. Tarim EA, Inevi AM, Ozkan I, Kecili S, Bilgi E, Baslar MS, et al. Microfluidic-based technologies for diagnosis, prevention, and treatment of COVID-19: recent advances and future directions. *Biomed Microdevices* 2023;**25**:10.
4. Cheng NN, Liu MZ, Li WT, Sun BY, Liu DD, Wang GQ, et al. Protein post-translational modification in SARS-CoV-2 and host interaction. *Front Immunol* 2023;**13**:1068449.
5. Lazarus JV, Wyka K, White TM, Picchio CA, Gostin LO, Larson HJ, et al. A survey of COVID-19 vaccine acceptance across 23 countries in 2022. *Nat Med* 2023;**29**:366−75.
6. Loo CY, Lee WH, Zhou QT. Recent advances in inhaled nanoformulations of vaccines and therapeutics targeting respiratory viral infections. *Pharm Res* 2023;**40**:1015−36.
7. Prabhakar PK, Khurana N, Vyas M, Sharma V, Batiha GE-S, Kaur H, et al. Aspects of nanotechnology for COVID-19 vaccine development and its delivery applications. *Pharmaceutics* 2023;**15**:451.
8. Le TT, Andreadakis Z, Kumar A, Román RG, Tollefsen S, Mayhew S. The COVID-19 vaccine development landscape. *Nat Rev Drug Discov* 2020;**19**:305−6.
9. Cheng CW, Wu CY, Wang SW, Chen JY, Kung CC, Liao KS, et al. Low-sugar universal mRNA vaccine against coronavirus variants with deletion of glycosites in the S2 or stem of SARS-CoV-2 spike messenger RNA (mRNA). *Proc Natl Acad Sci U S A* 2023;**120**:e2314392120.
10. Arevalo CP, Bolton MJ, Sage LV, Ye NQ, Furey C, Muramatsu H, et al. A multivalent nucleoside-modified mRNA vaccine against all known influenza virus subtypes. *Science* 2022;**378**:899−904.

11. LaTourette PC, Awasthi S, Desmond A, Pardi N, Cohen GH, Weissman D, et al. Protection against herpes simplex virus type 2 infection in a neonatal murine model using a trivalent nucleoside-modified mRNA in lipid nanoparticle vaccine. *Vaccine* 2020;**38**: 7409−13.
12. Uddin MN, Roni MA. Challenges of storage and stability of mRNA-Based COVID-19 vaccines. *Vaccine* 2021;**9**:1033.
13. Crommelin DJA, Anchordoquy TJ, Volkin DB, Jiskoot W, Mastrobattista E. Addressing the cold reality of mRNA vaccine stability. *J Pharm Sci US* 2021;**110**:997−1001.
14. Seaman CP, Kahn AL, Kristensen D, Steinglass R, Spasenoska D, Scott N, et al. Controlled temperature chain for vaccination in low- and middle-income countries: a realist evidence synthesis. *Bull World Health Org* 2022;**100**:491−502.
15. Eyawo O, Viens AM, Ugoji UC. Lockdowns and low- and middle-income countries: building a feasible, effective, and ethical COVID-19 response strategy. *Glob Health* 2021;**17**:13.
16. Arya J, Prausnitz MR. Microneedle patches for vaccination in developing countries. *J Control Release* 2016;**240**:135−41.
17. Freeman D, Lambe S, Yu LM, Freeman J, Chadwick A, Vaccari C, et al. Injection fears and COVID-19 vaccine hesitancy. *Psychol Med* 2023;**53**:1185−95.
18. Wang HH, Cui MT, Li SR, Wu F, Jiang SQ, Chen HB, et al. Perception and willingness toward various immunization routes for COVID-19 vaccines: a cross-sectional survey in China. *Front Public Health* 2023;**11**:1192709.
19. Chang H, Zheng MJ, Chew SWT, Xu CJ. Advances in the formulations of microneedles for manifold biomedical applications. *Adv Mater Technol* 2020;**5**:1900552.
20. Ray S, Wirth DM, Ortega-Rivera OA, Steinmetz NF, Pokorski JK. Dissolving microneedle delivery of a prophylactic HPV vaccine. *Biomacromolecules* 2022;**23**:903−12.
21. Straeten VA, Sarmadi M, Daristotle JL, Kanelli M, Tostanoski LH, Collins J, et al. A microneedle vaccine printer for thermostable COVID-19 mRNA vaccines. *Nat Biotechnol* 2024;**42**:510−7.
22. Pan YD, Liu LZ, Tian T, Zhao JX, Park CO, Lofftus SY, et al. Epicutaneous immunization with modified vaccinia ankara viral vectors generates superior T cell immunity against a respiratory viral challenge. *Npj Vaccines* 2021;**6**:1.
23. Li MC, Yang L, Wang CC, Cui MT, Wen ZY, Liao ZH, et al. Rapid induction of long-lasting systemic and mucosal immunity *via* thermostable microneedle-mediated chitosan oligosaccharide-encapsulated DNA nanoparticles. *ACS Nano* 2023;**17**:24200−17.
24. Anane-Adjei AB, Jacobs E, Nash SC, Askin S, Soundararajan R, Kyobula M, et al. Amorphous solid dispersions: utilization and challenges in preclinical drug development within astra zeneca. *Int J Pharm* 2022;**614**:121387.
25. Liu LZ, Zhong Q, Tian T, Dubin K, Athale SK, Kupper TS. Epidermal injury and infection during poxvirus immunization is crucial for the generation of highly protective T cell-mediated immunity. *Nat Med* 2010;**16**:224−7.
26. Kremer M, Suezer Y, Volz A, Frenz T, Majzoub M, Hanschmann KM, et al. Critical role of perforin-dependent $CD8^+$ T cell immunity for rapid protective vaccination in a murine model for human smallpox. *PLoS Pathog* 2012;**8**:e1002557.
27. Belongia EA, Naleway AL. Smallpox vaccine: the good, the bad, and the ugly. *Cli Med Res* 2003;**1**:87−92.
28. Schmidt ME, Knudson CJ, Hartwig SM, Pewe LL, Meyerholz DK, Langlois RA, et al. Memory CD8 T cells mediate severe immunopathology following respiratory syncytial virus infection. *PLoS Pathog* 2018;**14**:e1006810.
29. Gordon SN, Cecchinato V, Andresen V, Heraud JM, Hryniewicz A, Parks RW, et al. Smallpox vaccine safety is dependent on T cells and not B cells. *J Infect Dis* 2011;**203**:1043−53.
30. Kennedy JS, Frey SE, Yan LH, Rothman AL, Cruz J, Newman FK, et al. Induction of human T cell-mediated immune responses after primary and secondary smallpox vaccination. *J Infect Dis* 2004;**190**: 1286−94.
31. Schmidt ME, Varga SM. The CD8 T cell response to respiratory virus infections. *Front Immunol* 2018;**9**:678.
32. Lin SQ, Quan GL, Hou AL, Yang PP, Peng TT, Gu YK, et al. Strategy for hypertrophic scar therapy: improved delivery of triamcinolone acetonide using mechanically robust tip-concentrated dissolving microneedle array. *J Control Release* 2019;**306**:69−82.
33. Li MC, Chen JS, Liu YJ, Zhao J, Li YJ, Hu YQ, et al. Rational design of AAVrh10-vectored ACE2 functional domain to broadly block the cell entry of SARS-CoV-2 variants. *Antivir Res* 2022;**205**:105383.
34. Carrillo-Conde B, Song EH, Chavez-Santoscoy A, Phanse Y, Ramer-Tait AE, Pohl NLB, et al. Mannose-functionalized "pathogen-like" polyanhydride nanoparticles target c-type lectin receptors on dendritic cells. *Mol Pharm* 2011;**8**:1877−86.
35. Loizidou EZ, Inoue NT, Ashton-Barnett J, Barrow DA, Allender CJ. Evaluation of geometrical effects of microneedles on skin penetration by CT scan and finite element analysis. *Eur J Pharm Biopharm* 2016; **107**:1−6.
36. Olatunji O, Das DB, Garland MJ, Belaid L, Donnelly RF. Influence of array interspacing on the force required for successful microneedle skin penetration: theoretical and practical approaches. *J Pharm Sci US* 2013;**102**:1209−21.
37. Gong L, Zhang YY, Wang LL, Zhao XY, Wang LC, Qiu XQ, et al. Advancing vaccine development: evaluation of a mannose-modified lipid nanoparticle-based candidate for African swine fever p30 mRNA vaccine eliciting robust immune response in mice. *Int J Biol Macromo* 2024;**270**:132432.
38. Lederer K, Castaño D, Atria GD, Oguin TH, Wang S, Manzoni TB, et al. SARS-CoV-2 mRNA vaccines foster potent antigen-specific germinal center responses associated with neutralizing antibody generation. *Immunity* 2020;**53**:1281−95.e5.
39. Cao FQ, Peng S, An YL, Xu K, Zheng TY, Dai LP, et al. Inside-out assembly of viral antigens for the enhanced vaccination. *Sig Transduct Target Ther* 2023;**8**:189.
40. Yu Y, Wang J, Wu MX. Microneedle-mediated immunization promotes lung $CD8^+$ T-cell immunity. *J Invest Dermatol* 2023;**143**. 1983-92.e3.
41. Bull NC, Stylianou E, Kaveh DA, Pinpathomrat N, Pasricha J, Harrington-Kandt R, et al. Enhanced protection conferred by mucosal BCG vaccination associates with presence of antigen-specific lung tissue-resident PD-$1^+$ KLRG1− $CD4^+$ T cells. *Mucosal Immunol* 2019;**12**:555−64.
42. Cho E, Cho W, Cha KH, Park J, Kim MS, Kim JS, et al. Enhanced dissolution of megestrol acetate microcrystals prepared by antisolvent precipitation process using hydrophilic additives. *Int J Pharm* 2010; **396**:91−8.
43. Alam MA, Ali R, Al-Jenoobi FI, Al-Mohizea AM. Solid dispersions: a strategy for poorly aqueous soluble drugs and technology updates. *Eur J Pharm Biopharm* 2012;**9**:1419−40.
44. Zhang KR, Yu HX, Luo Q, Yang SS, Lin X, Zhang Y, et al. Increased dissolution and oral absorption of itraconazole/soluplus extrudate compared with itraconazole nanosuspension. *Eur J Pharm Biopharm* 2013;**85**:1285−92.
45. Merisko-Liversidge E, Liversidge GG. Nanosizing for oral and parenteral drug delivery: a perspective on formulating poorly-water soluble compounds using wet media milling technology. *Adv Drug Deliv Rev* 2011;**63**:427−40.
46. Yang H, Teng F, Wang P, Tian B, Lin X, Hu X, et al. Investigation of a nanosuspension stabilized by Soluplus® to improve bioavailability. *Int J Pharm* 2014;**477**:88−95.
47. Yu CC, Zhang CG, Guan XF, Yuan D. The solid dispersion of resveratrol with enhanced dissolution and good system physical stability. *J Drug Deliv Sci Tec* 2023;**84**:104507.
48. Wen XM, Deng ZY, Xu YF, Yan GQ, Deng X, Wu LQ, et al. Preparation and *in vitro/in vivo* evaluation of orally disintegrating/modified-release praziquantel tablets. *Pharmaceutics* 2021;**13**:1567.
49. Bray M. Understanding smallpox vaccination. *J Infect Dis* 2011;**203**: 1037−9.

50. Terajima M, Cruz J, Leporati AM, Demkowicz WE, Kennedy JS, Ennis FA. Identification of vaccinia $CD8^+$ T-cell epitopes conserved among vaccinia and variola viruses restricted by common MHC class I molecules, HLA-A2 or HLA-B7. *Hum Immunol* 2006;**67**:512−20.
51. Martin MD, Badovinac VP. Defining memory CD8 T cell. *Front Immunol* 2018;**9**:2692.
52. Zaric MJ, Becker PD, Hervouet C, Kalcheva P, Doszpoly A, Blattman N, et al. Skin immunisation activates an innate lymphoid cell−monocyte axis regulating $CD8^+$ effector recruitment to mucosal tissues. *Nat Commun* 2019;**10**:2214.
53. Liu LZ, Fuhlbrigge RC, Karibian K, Tian T, Kupper TS. Dynamic programing of $CD8^+$ T cell trafficking after live viral immunization. *Immunity* 2006;**25**:511−20.
54. Masopust D, Choo D, Vezys V, Wherry EJ, Duraiswamy J, Akondy R, et al. Dynamic T cell migration program provides resident memory within intestinal epithelium. *J Exp Med* 2010;**207**: 553−64.
55. Shin H, Iwasaki A. A vaccine strategy that protects against genital herpes by establishing local memory T cells. *Nature* 2012;**491**: 463−7.